Supplementary Information

Dynamic piezoelectric effect to promote electrosynthesis of hydrogen peroxide

Hongyuan Yang,[a,b,+] Jie Wu,[a,+] Zhengran Chen,[c,+] Zou Kai,[c] Ruihong Liang,[c] Zhenhui Kang,*[a] Prashanth W. Menezes*[b,d] and Ziliang Chen*[a,b]

[a.] Institute of Functional Nano and Soft Materials (FUNSOM), Jiangsu Key Laboratory for Carbon-based Functional Materials and Devices, Joint International Research Laboratory of Carbon-Based Functional Materials and Devices, Soochow University, Suzhou 215123, P. R. China

[b.] Department of Chemistry: Metalorganics and Inorganic Materials, Technical University of Berlin, Straße des 17 Juni 135. Sekr. C2, Berlin 10623, Germany

[c.] Key Laboratory of Inorganic Functional Materials and Devices, Shanghai Institute of Ceramics, Chinese Academy of Sciences, 588 Heshuo Road, Jiading District, Shanghai 201800, P. R. China

[d.] Materials Chemistry Group for Thin Film Catalysis – CatLab, Helmholtz-Zentrum Berlin für Materialien und Energie, Albert-Einstein-Str. 15, Berlin 12489, Germany

[+] H. Yang, J. Wu, and Z. R. Chen contributed equally in this work.

* E-mail: zhkang@suda.edu.cn; prashanth.menezes@mailbox.tu-berlin.de; prashanth.menezes@helmholtz-berlin.de; zlchen@suda.edu.cn

Supplementary experimental details

For investigating the piezoelectric capability of the ground ceramic catalysts, they were firstly deposited on FTO glass (insulating side) slides by mixing the ground ceramic powders (around 4 mg) with the 300 μL deionized water, 650 μL ethanol, and 50 μL Nafion. The mass loadings were controlled in the same way. Similarly, to perform the post-ORR characterizations on powder PZT-0 and PZT-2 catalysts, through the same procedure, such two powder samples were deposited on carbon paper first. Hereafter, a 12 h chronoamperometry (CA) run at 0.4 V *vs.* reversible hydrogen electrode (RHE) was applied in the O_2-saturated three-electrode where the carbon paper-supporting catalyst, Hg/HgO electrode, and graphite rod served as working electrode, reference electrode, and counter electrode, respectively. Of note, the 0.1 M KOH electrolyte (same volume in the same electrolyzer) for both PZT catalysts was both stirred at the rate of 1600 rpm, the same as the rotating speed of the rotating-ring disk electrode (RRDE) for the ORR measurements, which aimed to make sure the pressures (per geometric area) applied on the deposited PZT catalysts were almost identical. Consequently, enough post-ORR samples were acquired for the subsequent characterizations. In the almost same electrochemistry environment, a 12 h CA treatment at a fixed potential of 0.4 V (*vs.* RHE) was also applied to the starting ceramic tablet of polarized PZT-2 sample, aiming to probe the stability of the piezoelectric behavior of the polarized PZT ceramics after ORR.

Besides, the *ex-situ* and quasi *in-situ* Raman tests were also carried out to determine if the piezoelectric response during ORR would influence the phase of PZT

catalysts. For *ex-situ* examinations, the PZT-0 and PZT-2 powders were deposited on FTO glass substrates using the same procedure as that performed for the abovementioned piezoelectricity estimations. Next, for the quasi *in-situ* measurements, the as-deposited PZT-0 and PZT-2 films were activated through 12 h ORR CA at 0.4 V *vs.* RHE, followed by being freeze-quenched at the same potential using liquid N_2 under vigorous Ar gas flow, and stored in the liquid N_2.
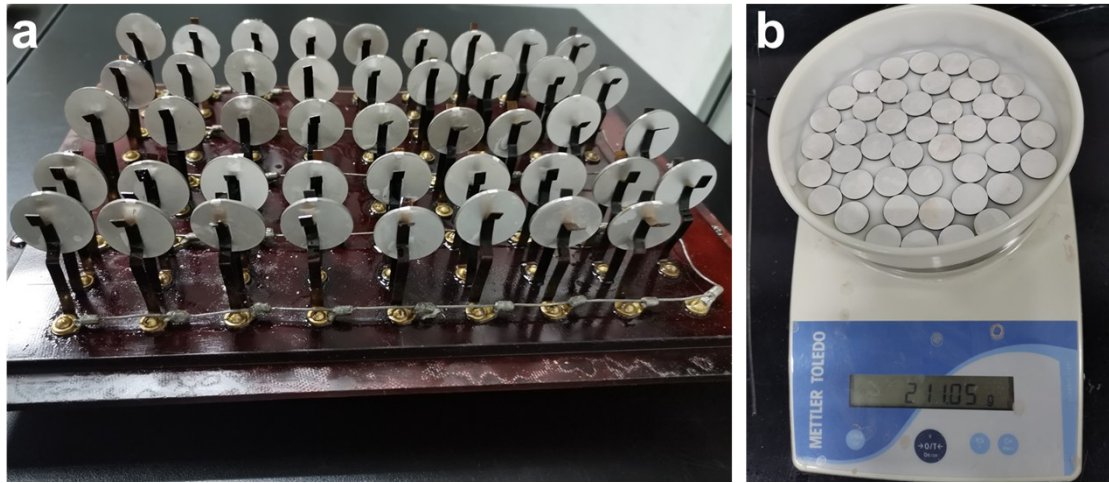
Fig. S1. The optical photos of (a) the as-prepared ceramic (PZT) tablets under polarization in one-batch treatment and (b) their corresponding total mass.

Table S1. Piezoelectric constants (d_{33}) of PZT-0, 1.5, 2, and 2.5 in the form of starting ceramic tablets and ground powders (deposited on insulating side of FTO slide),

Sample	Polarization electric field (kV mm^{-1})	d_{33} (pC N^{-1}) Tablet	d_{33} (pC N^{-1}) Powder
PZT-0	0	0	0
PZT-1.5	1.5	-25	-0.6
PZT-2	2	-50	-1.1
PZT-2.5	2.5	-130	-1.7

respectively, treated under different polarization electric fields.

d_{33} results prove that polarized PZT powder catalysts can still preserve remarkable piezoelectric activity with the same trend as that of their starting ceramic tablets treated under different electric fields, while not any piezoelectric behavior can be found in PZT-0 powder.
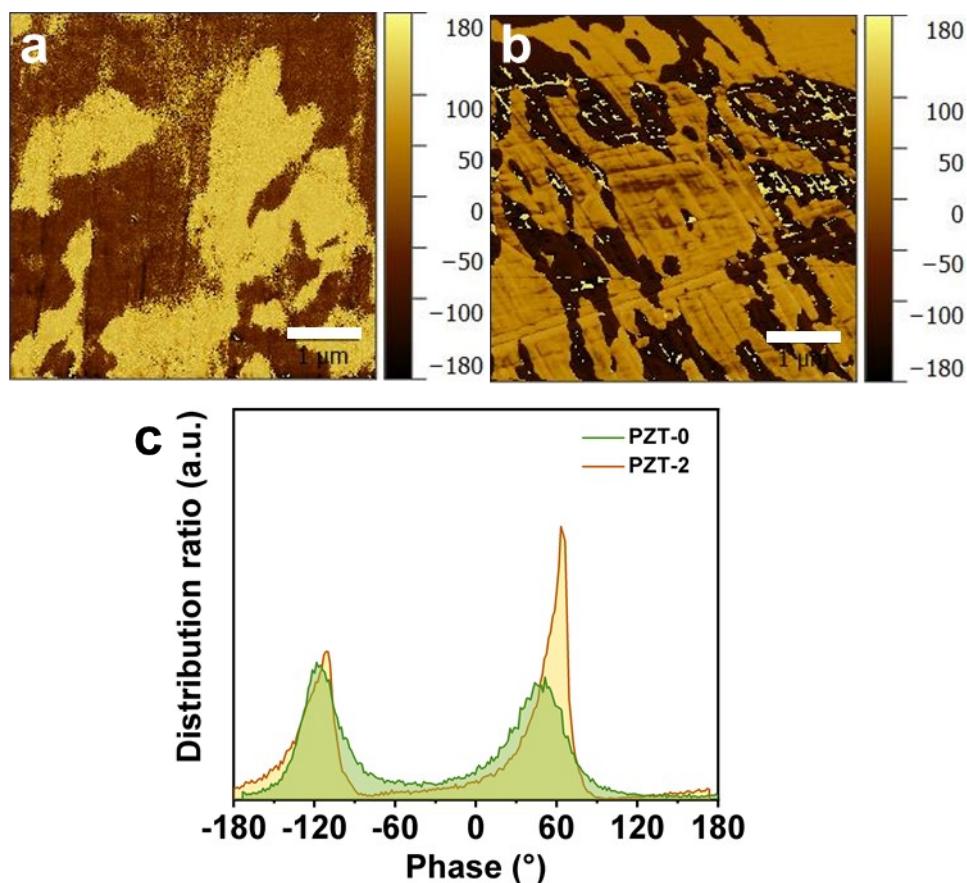
Fig. S2. Piezoresponse force microscopy (PFM) images of (a) unpolarized PZT-0 tablet and (b) polarized PZT-2 tablet, as well as (c) their corresponding phase distribution diagram. Scale bar: 1 μm.

To detect the distribution of electric domains inside the PZT tablets before and after polarization, we performed the PFM characterizations. Apparently, after the polarizing treatment, distinctly more concentrated and ordered electric domain distribution can be found in the PZT-2 ceramic tablet, demonstrating its piezoelectric performance was accordingly enhanced. Hence, combining the d_{33} results with PFM findings, it can be concluded that polarized PZT-2 ceramic tablet was endowed with a strong piezoelectric response compared with unpolarized PZT-0 one (non-piezoelectric), which were both then ground into powders, serving as the ORR catalysts.

Table S2. Simulated surface potentials of the non-piezoelectric PZT-0 as well as piezoelectric PZT-1.5, 2, and 2.5 models under the stresses induced by fluid rotating (the same speed as the RRDE rotating value for ORR measurement).

Sample	Surface potential (V)
PZT-0	0
PZT-1.5	-6.98 x 10^{-4}
PZT-2	-7.07 x 10^{-4}
PZT-2.5	-7.34 x 10^{-4}
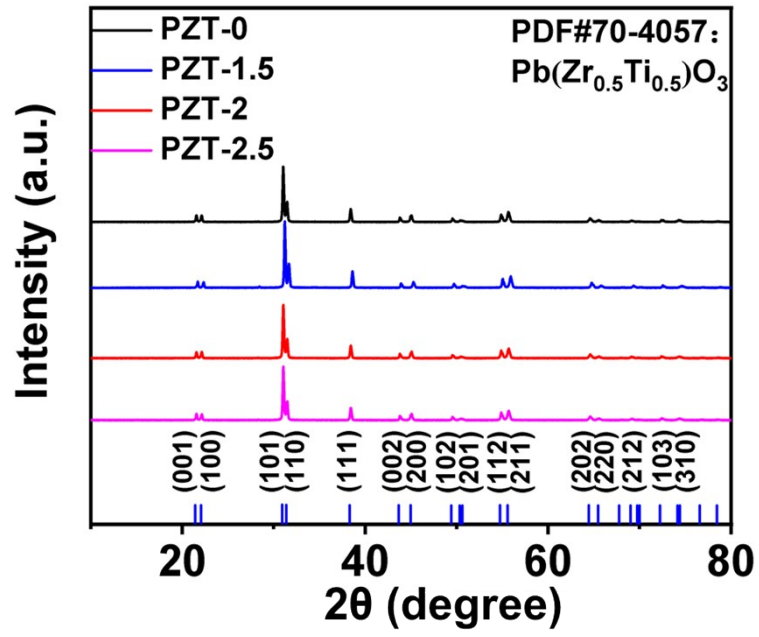
Fig. S3. XRD patterns of the unpolarized PZT-0, as well as polarized PZT-1.5, 2, and

2.5 powder catalysts. All the samples exhibited the same XRD patterns which can be

well-indexed to the $Pb(Zr_{0.5}Ti_{0.5})O_3$ phase regardless of the strength of polarization.
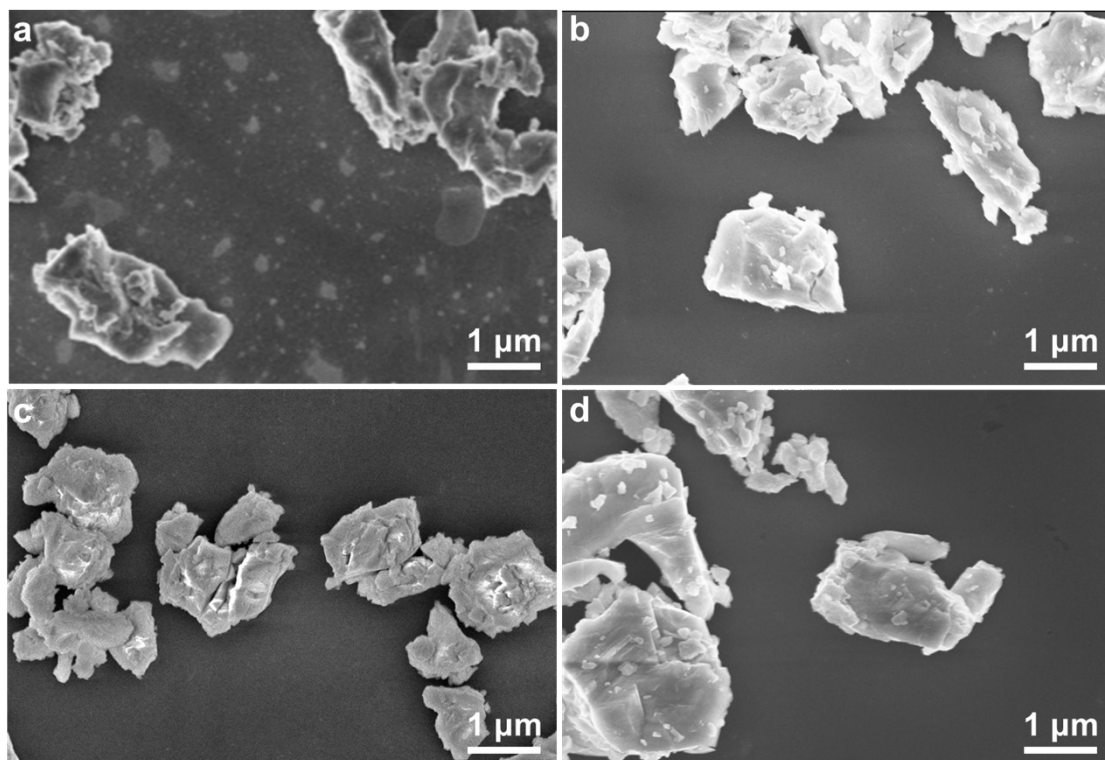
Fig. S4. FESEM images of (a) unpolarized PZT-0, as well as polarized (b) PZT-1.5, (c)

PZT-2, and (d) PZT-2.5 powder catalysts.

Table S3. Elemental content of unpolarized PZT-0, as well as polarized PZT-1.5, 2, and 2.5 powder catalysts determined by inductively coupled plasma-optical emission spectrometer (ICP-OES).

Sample	Pb	Zr	Ti
PZT-0	1	0.49	0.49
PZT-1.5	1	0.48	0.48
PZT-2	1	0.48	0.47
PZT-2.5	1	0.454	0.486
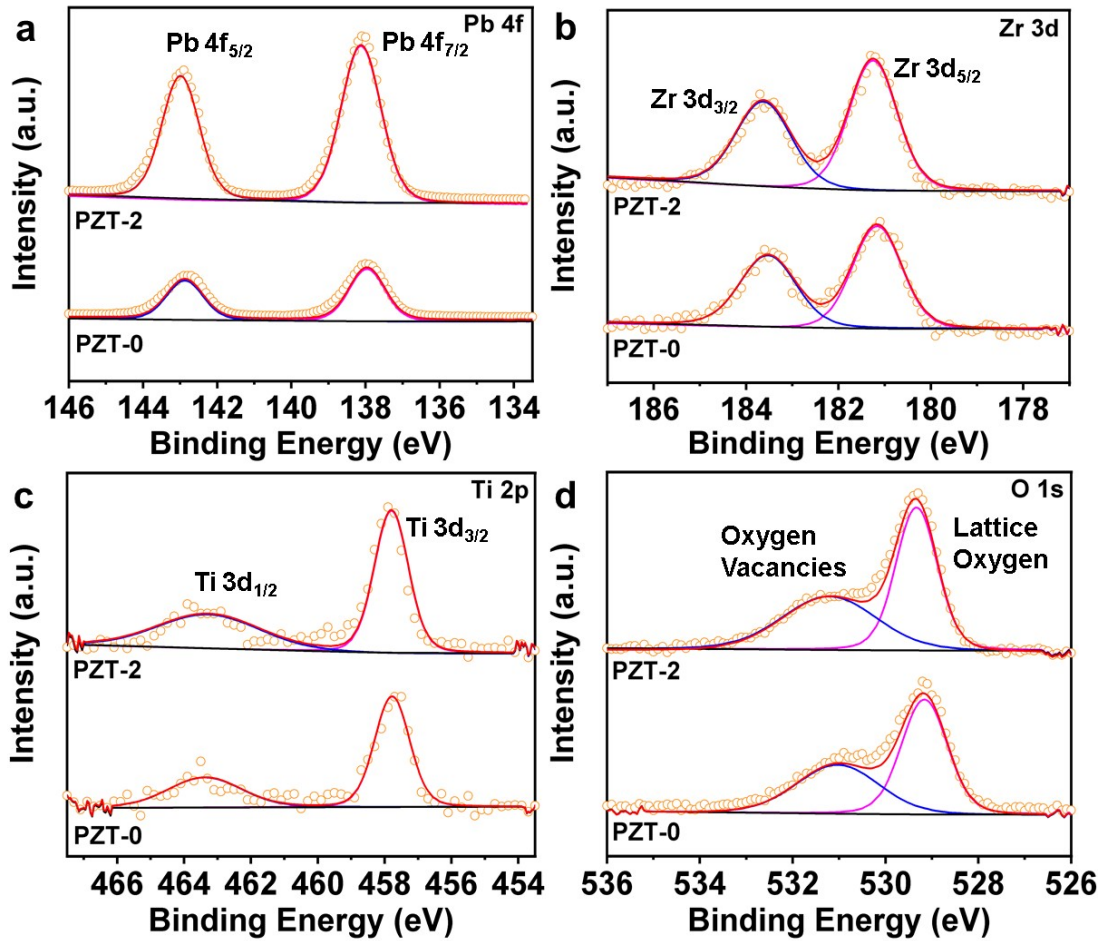
Fig. S5. High-resolution (a) Pb 4f, (b) Zr 3d, (c) Ti 2p, and (d) O 1s XPS spectra of non-piezoelectric PZT-0 and piezoelectric PZT-2 powder catalysts.

Compared with the XPS spectra of the PZT sample reported in the previous work, an extremely similar fitted peak position confirmed the successful formation of the lead zirconate titanate phase for both PZT-0 and PZT-2 samples.[1] On the other hand, no matter whether the PZT powder catalysts presented piezoelectric feature, their XPS peaks were located at the almost same binding energy, meaning the polarization treatment (to endow the PZT with piezoelectricity) did not obviously influence the chemical states. Note that we magnified all the XPS spectra of PZT-0 in this figure by 2.5 times for more clear observation and comparison.
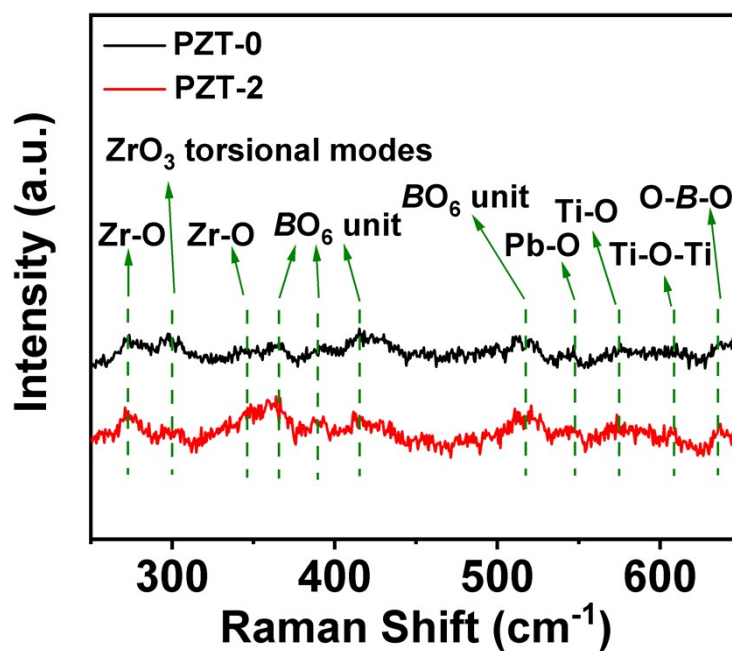
Fig. S6. Raman spectra of non-piezoelectric PZT-0 and piezoelectric PZT-2 powder catalysts.

On one hand, according to the previous reports on the PZT materials, we can confirm the formation of lead zirconate titanate phase for both PZT-0 and PZT-2,[1–7] consistent with the above XRD, ICP-OES, and XPS results. On the other hand, PZT-0 and PZT-2 nearly exhibited the same Raman band position, suggesting the identical surface coordination environment, which is independent of the piezoelectricity enabled by additional polarization. Note for a clearer observation and comparison, the baselines of these two curve data were subtracted.
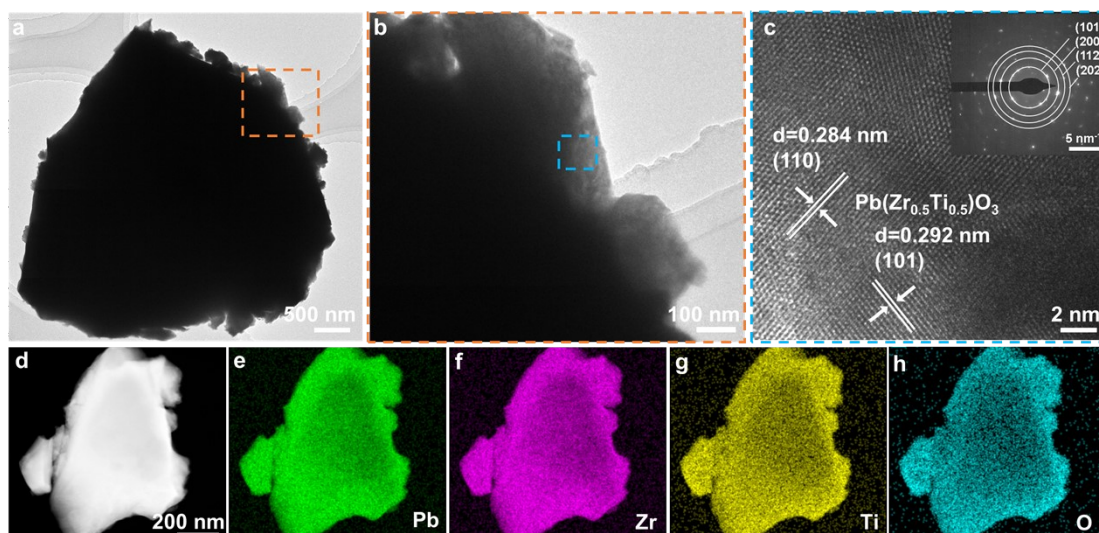
Fig. S7. (a) TEM image, and (b) the high-magnification, as well as (c) the high-resolution TEM (HRTEM) image with the inset of the associated selected area electron diffraction (SAED) for non-piezoelectric PZT-0 powder catalyst. (d) The high angle annular dark field-scanning TEM (HAADF-STEM) pattern of representative PZT-0 particle together with the corresponding elemental mapping images of (e) Pb, (f) Zr, (g) Ti, and (h) O.

The identification of the lattice distances and the assignment of the crystalline facets reflected by the above HRTEM and SAED data confirmed the successful formation of the lead zirconate titanate phase. Moreover, the HAADF-STEM pattern and the associated elemental mapping images illustrated the homogenous distribution of all the elements for PZT-0.
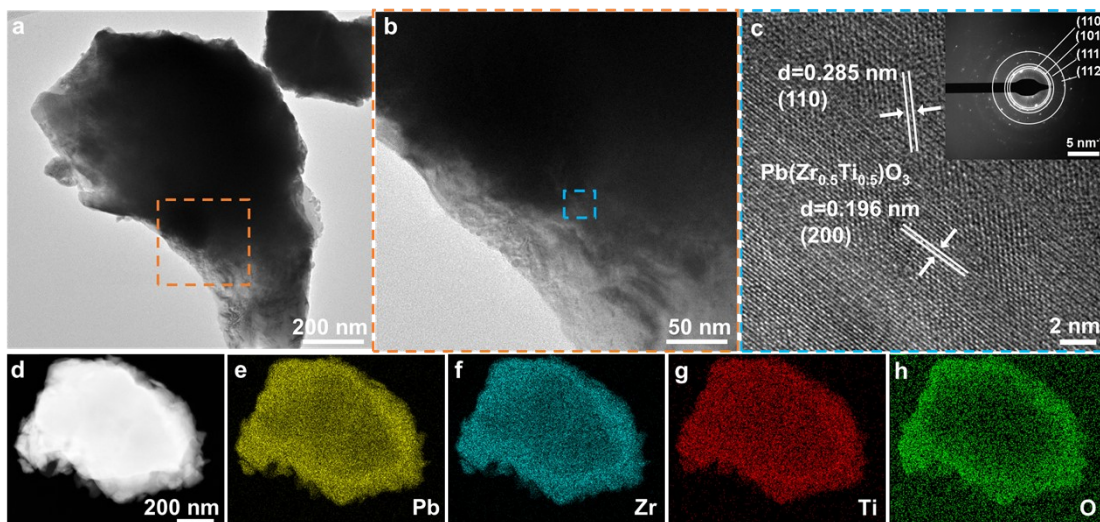
Fig. S8. (a) TEM image, and (b) the high-magnification, as well as (c) the HRTEM image with the inset of the associated SAED for piezoelectric PZT-2 powder catalyst. (d) The HAADF-STEM pattern of representative PZT-0 particle together with the corresponding elemental mapping images of (e) Pb, (f) Zr, (g) Ti, and (h) O.

In analogy to PZT-0, the HRTEM, SAED, HAADF-STEM and the associated elemental mapping data in this figure verify the formation of successful formation of the lead zirconate titanate phase with even elemental distribution for PZT-2. More importantly, the polarizing treatment towards PZT did not pronouncedly influence its crystalline phase and elemental presence.

Note that considering the unrivaled electrocatalytic $2e^-$ ORR performance (elaborated in the section "**ORR performances of PZT ceramic electrocatalysts**" of the main text), we specially selected the PZT-2 powder catalyst as the representative of polarized PZT samples for more detailed comparison with unpolarized PZT-0 on the aspects of morphology, crystallinity, chemical state, as well as elemental composition and distribution (Figs. S3−S8 and Table S3).
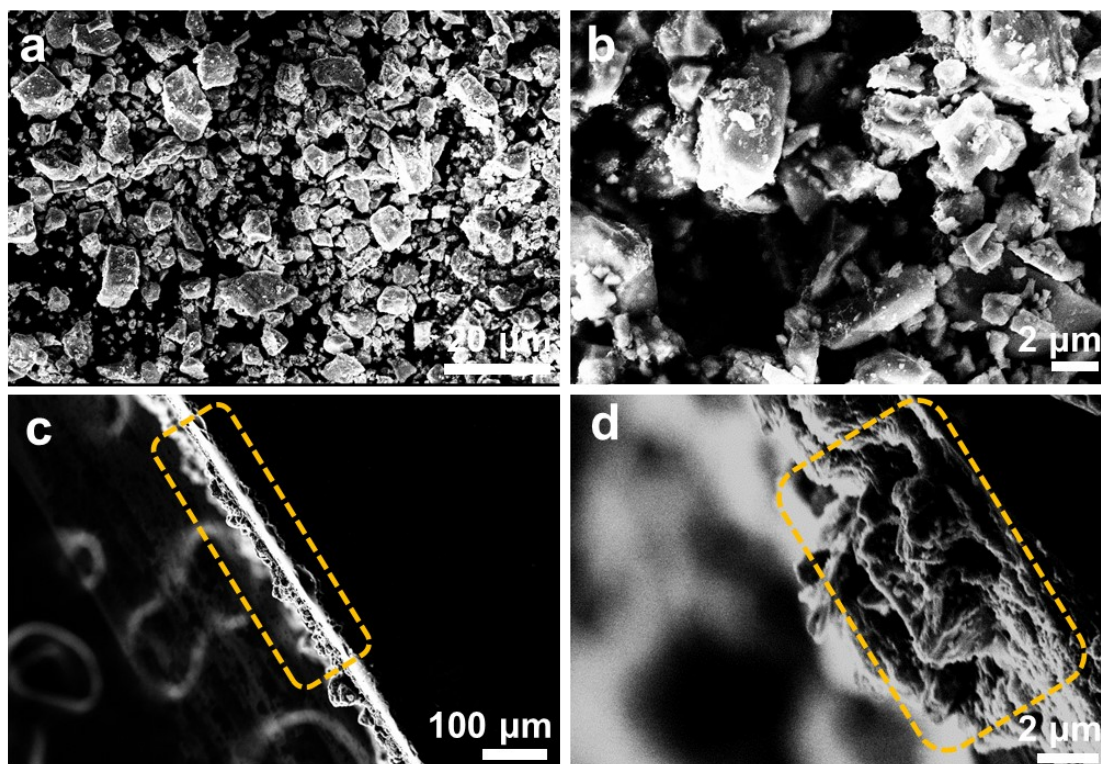
Fig. S9. FESEM images of the representative PZT-2 catalysts powders which were deposited on the glassy carbon plate: (a,b) top view and (c,d) side view.
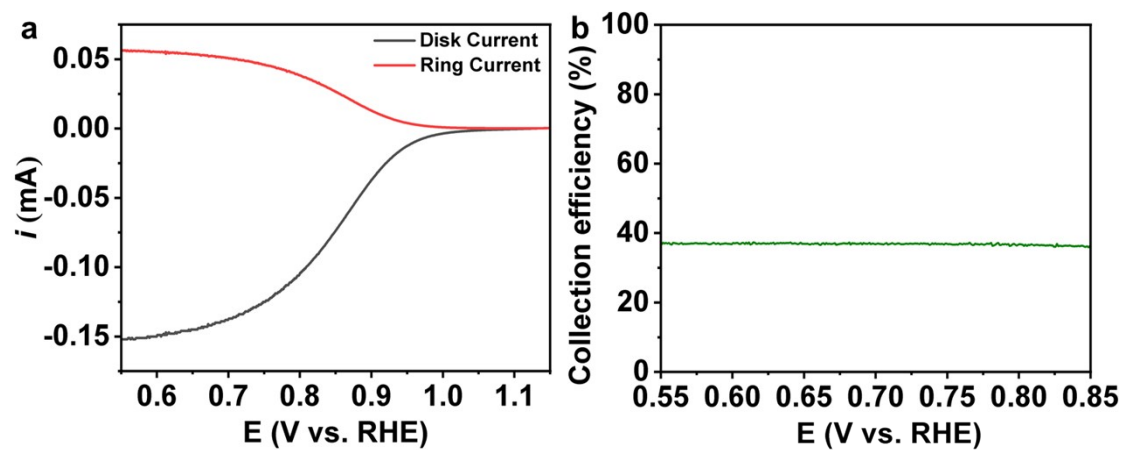
Fig. S10. Calibration towards the collection efficiency (*N*) of bare RRDE in Ar-saturated 1 M KNO$_3$ dissolved with 2 mM K$_3$[Fe(CN)$_6$]. (a) RRDE voltammograms recorded by performing linear sweep voltammetry (LSV) on disk from 0.55 to 1.15 V (*vs*. RHE) at 10 mV s^{-1} at 1600 rpm while holding the ring at 1.14 V (*vs*. RHE). (b) The associated *N* of RRDE voltammograms as a function of the potential.
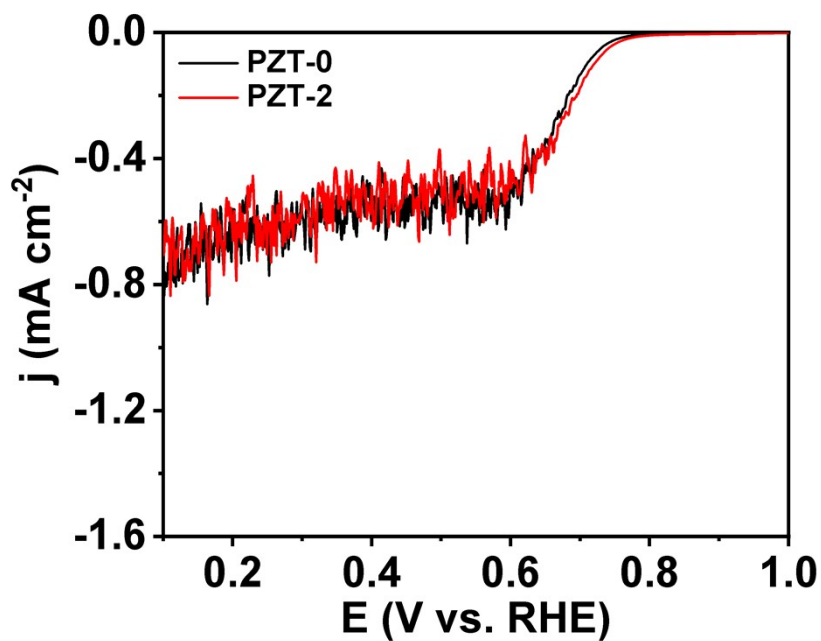
Fig. S11. LSV curves of unpolarized PZT-0 and polarized PZT-2 using the non-rotating

RRDE at the scan rate of 1 mV s^{-1}.

The similar LSV curves of these two samples under a steady measurement environment

(accordingly no external forces were induced towards the surface of the PZT samples)

confirmed that the enhanced ORR capability of polarized PZT-2 originated from its

distinct piezoelectric response.

Table S4. The comparison of ORR performance of PZT-2 measured *via* RRDE at 1600 rpm with those of reported oxides-based and other kinds of advanced 2e⁻ ORR catalysts (*e.g.*, sulfides and selenides-based ones) (at 0.5~0.4 V *vs.* RHE).

Material	Electrolyte	Selectivity	Stability	Ref.
$Pb(NiWMnNbZrTi)_{1/6}O_3$	0.1 M KOH	~96%	>12 h	[1]
Fe_3O_4/Printex	1 M KOH	~70%	5.5 h	[8]
$a\text{-}TiO_{2-x}$/TiC	0.1 M KOH	~93%	12 h	[9]
$Sr_{0.7}Na_{0.3}Si_{0.95}Ni_{0.05}O_{3-\delta}$	0.1 M KOH	<80%	/	[10]
Nb_2O_5-rGO	0.1 M NaOH	~75%	5.5 h	[11]
Zr-rGO	0.1 M NaOH	~80%	6 h	[12]
$BaSm_2O_4$-vulcan carbon	0.1 M KOH	~93%	~3.5 h	[13]
CuO_x/G-30	1 M KOH	<85%	>8 h	[14]
4% CeO_2/C	1 M NaOH	~88%	/	[15]
NiO/NiFe-MOF	0.1 M KOH	~98%	11 h	[16]
Ni-LDH C/CNSs	0.1 M KOH	~87%	16 h	[17]
$Ba_{0.5}Sr_{0.5}Fe_{0.95}Cu_{0.05}O_{3-\delta}$	0.1 M KOH	<70%	/	[18]
Ta_2O_5/C	0.1 M K_2SO_4[a]	~83.2%	/	[19]
$Ni_2Mo_4S_8$	0.1 M KOH	~98%	10 h	[20]
F-WS_2	0.1 M KOH	<85%	8 h	[21]
ZnS@C	0.1 M KOH	<88%	15 h	[22]
N-$NiCo_2S_4$/CP	0.1 M KOH	~90%	/	[23]
Ti–ZnCoS HSS	0.1 M KOH	~98%[b]	12 h	[24]
Cu_7Se_4	0.1 M KOH	~94%	1400 cycles	[25]
$CoSe_2$ NS/CC	0.1 M KOH	~92%	10 h	[26]
$CuCo_{0.8}Ni_{1.2}S_4$	0.05 M H_2SO_4	<70%	1.5 h	[27]
CoS_2	0.05 M H_2SO_4	~70%	1 h	[28]
$CoSe_2$	0.05 M H_2SO_4	>95%	~5 h	[29]

O-CNTs	0.1 M KOH	~90%	10 h	[30]
Au–Pt–Ni	0.1 M KOH	~95%	10 h	[31]
Fe-CNT	0.1 M KOH	~87%	>8 h	[32]
Co−N−C	0.1 M KOH	60−70%	6 h	[33]
S-NiP$_4$Mo$_6$	0.1 M KOH	~97%	/	[34]
Ni-N$_2$O$_2$/C	0.1 M KOH	~96%	8 h[c]	[35]
PZT-0	0.1 M KOH	~82%	>12 h	This work
PZT-2	0.1 M KOH	~98%	>12 h	This work

[a]pH=2; [b]at the potential region from 0.8~0.55 V *vs.* RHE; [c]at the three-phase flow cell electrolytic device
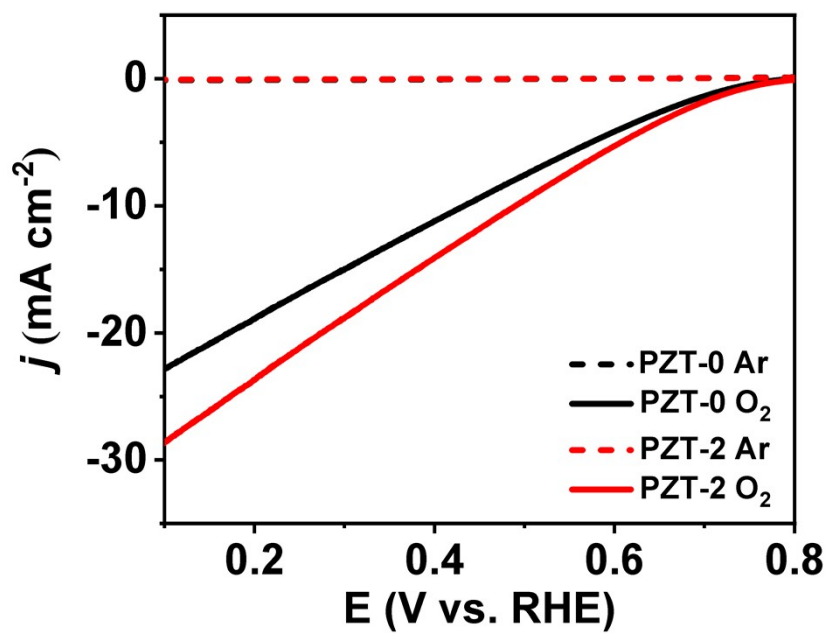
Fig. S12. LSV curves obtained from an assembled H-type electrolyzer containing O_2 and Ar-saturated 0.1 M KOH[1], where PZT-0 and PZT-2 supported on carbon paper served as the working electrode.
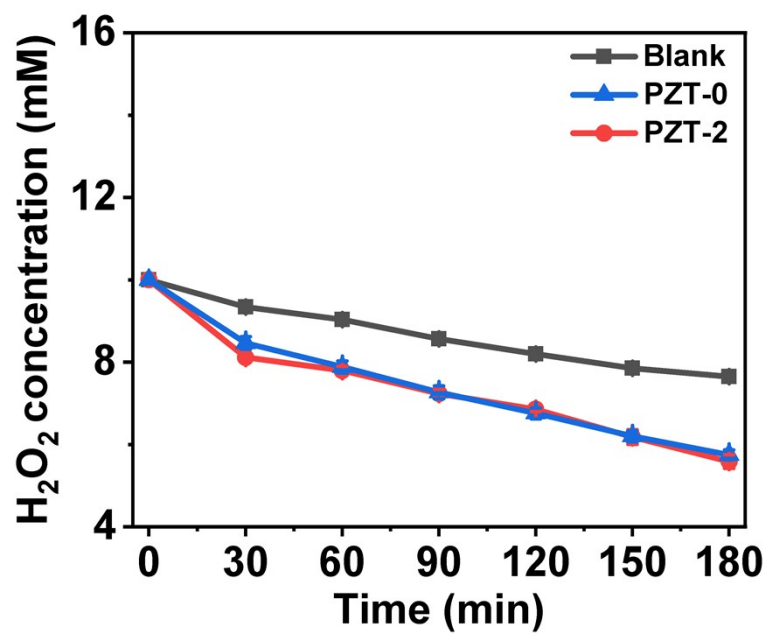
Fig. S13. Peroxide disproportionation reaction (PDR) measurements. 5 mg PZT-0 and PZT-2 powders were added into 20 mL 0.1 M KOH containing 10 mM H_2O_2, respectively. For a better comparison, PDR measurement was also investigated in the blank reaction solution without the addition of catalysts.

Table S5. d_{33} of U-Pb(Zr$_{0.4}$Ti$_{0.6}$)O$_3$, U-Pb(Zr$_{0.3}$Ti$_{0.7}$)O$_3$, P-Pb(Zr$_{0.4}$Ti$_{0.6}$)O$_3$, and P-

Sample	Polarization electric field (kV mm^{-1})	d_{33} (pC N^{-1})
U-Pb(Zr$_{0.4}$Ti$_{0.6}$)O$_3$	0	0
U-Pb(Zr$_{0.3}$Ti$_{0.7}$)O$_3$	3.1	-50
P-Pb(Zr$_{0.4}$Ti$_{0.6}$)O$_3$	0	0
P-Pb(Zr$_{0.3}$Ti$_{0.7}$)O$_3$	2.7	-50

Pb(Zr$_{0.3}$Ti$_{0.7}$)O$_3$ ceramic tablets treated under different polarization electric fields.

Through adjusting the polarization degree of the external electric fields, the d_{33} value of PZT ceramics with different atomic ratios of Zr/Ti turned out to be the same, meaning the identical piezoelectric responses triggered under the same dynamic ORR measurements.
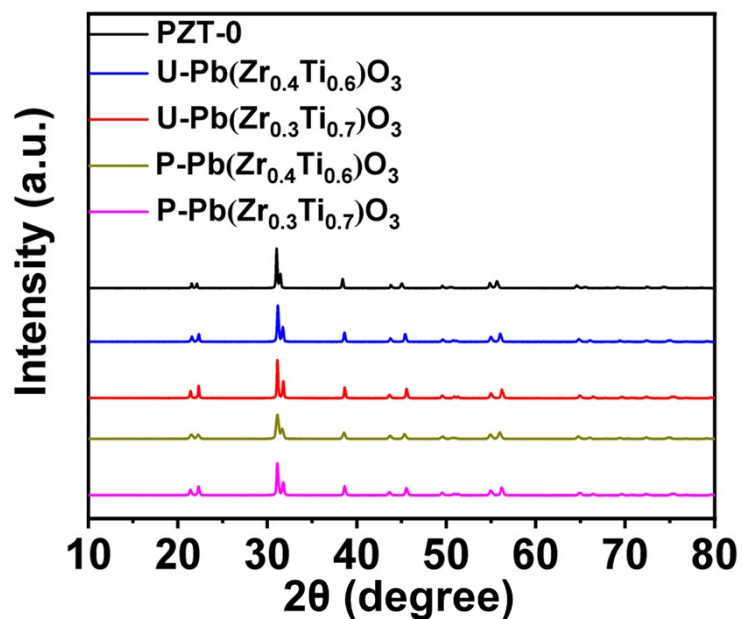
Fig. S14. XRD patterns of various PZT ceramic powder catalysts, including PZT-0 (*i.e.*, the unpolarized $Pb(Zr_{0.5}Ti_{0.5})O_3$), $U\text{-}Pb(Zr_{0.4}Ti_{0.6})O_3$ and $U\text{-}Pb(Zr_{0.3}Ti_{0.7})O_3$ before polarizing, as well as $P\text{-}Pb(Zr_{0.4}Ti_{0.6})O_3$ and $P\text{-}Pb(Zr_{0.3}Ti_{0.7})O_3$ after polarizing. Within the atomic ratio of Zr/Ti ranging from 0.5/0.5 to 0.3/0.7, the as-prepared PZT ceramics crystallized in the same space group of P4mm (No. 99) (PDF # 70−4057).[36,37] Moreover, the crystalline structure as that of PZT with an atomic ratio ≈ 0.4/0.6 and 0.3/0.7 did not change after polarizing.
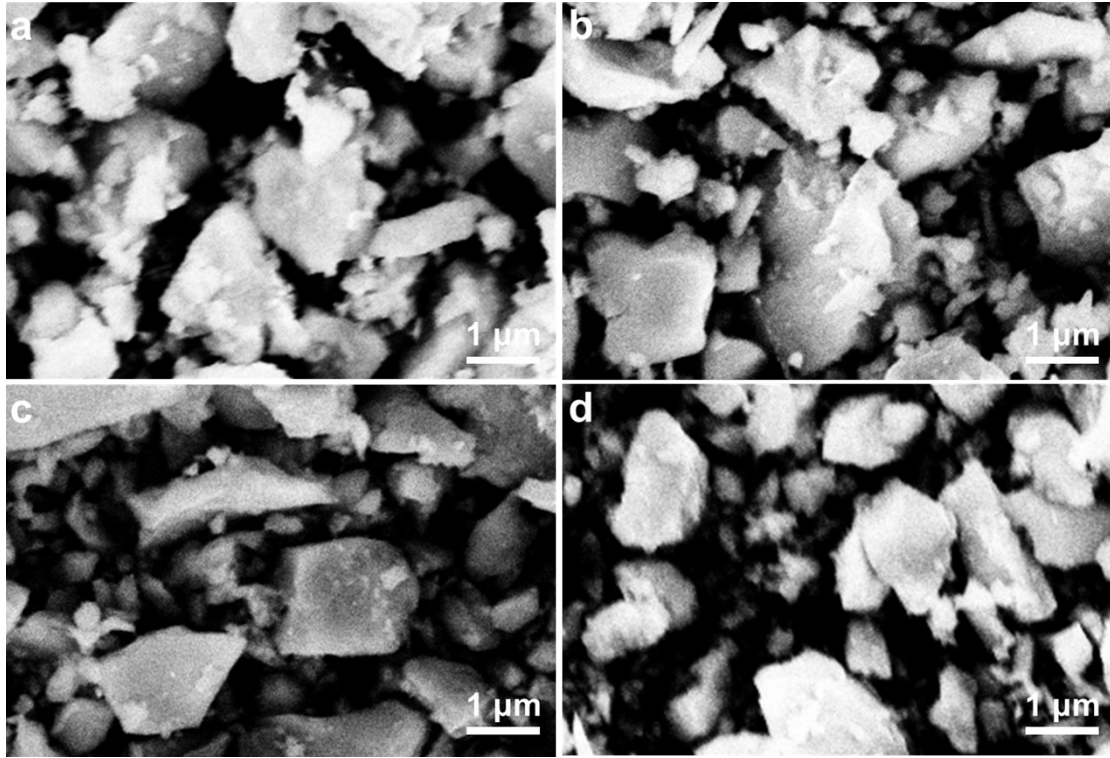
Fig. S15. FESEM images of the non-piezoelectric (a) U-Pb(Zr$_{0.4}$Ti$_{0.6}$)O$_3$ and (b) U-Pb(Zr$_{0.3}$Ti$_{0.7}$)O$_3$, as well as the piezoelectric (c) P-Pb(Zr$_{0.4}$Ti$_{0.6}$)O$_3$ (d) P-Pb(Zr$_{0.3}$Ti$_{0.7}$)O$_3$ powder catalysts.

Table S6. Elemental content of non-piezoelectric U-Pb(Zr$_{0.4}$Ti$_{0.6}$)O$_3$ and U-Pb(Zr$_{0.3}$Ti$_{0.7}$)O$_3$, as well as piezoelectric P-Pb(Zr$_{0.4}$Ti$_{0.6}$)O$_3$ and P-Pb(Zr$_{0.3}$Ti$_{0.7}$)O$_3$ powder catalysts determined by inductively coupled plasma-optical emission spectrometer (ICP-OES).

Sample	Pb	Zr	Ti
U-Pb(Zr$_{0.4}$Ti$_{0.6}$)O$_3$	1	0.36	0.58
U-Pb(Zr$_{0.3}$Ti$_{0.7}$)O$_3$	1	0.27	0.66
P-Pb(Zr$_{0.4}$Ti$_{0.6}$)O$_3$	1	0.37	0.58
P-Pb(Zr$_{0.3}$Ti$_{0.7}$)O$_3$	1	0.27	0.68
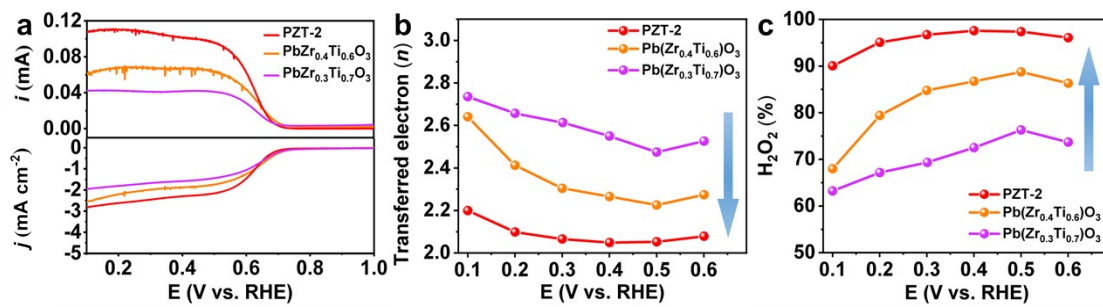
Fig. S16. (a) LSV curves of PZT-2, P-Pb($Zr_{0.4}Ti_{0.6}$)O_3 and P-Pb($Zr_{0.3}Ti_{0.7}$)O_3 recorded at 1600 rpm with the scan rate of 10 mV s^{-1} (bottom part), accompanied by the associated H_2O_2 current on the ring electrode (upper part). (b) The calculated n, and (c) selectivity of H_2O_2 within the potential ranging from 0.6 to 0.1 V (*vs.* RHE).
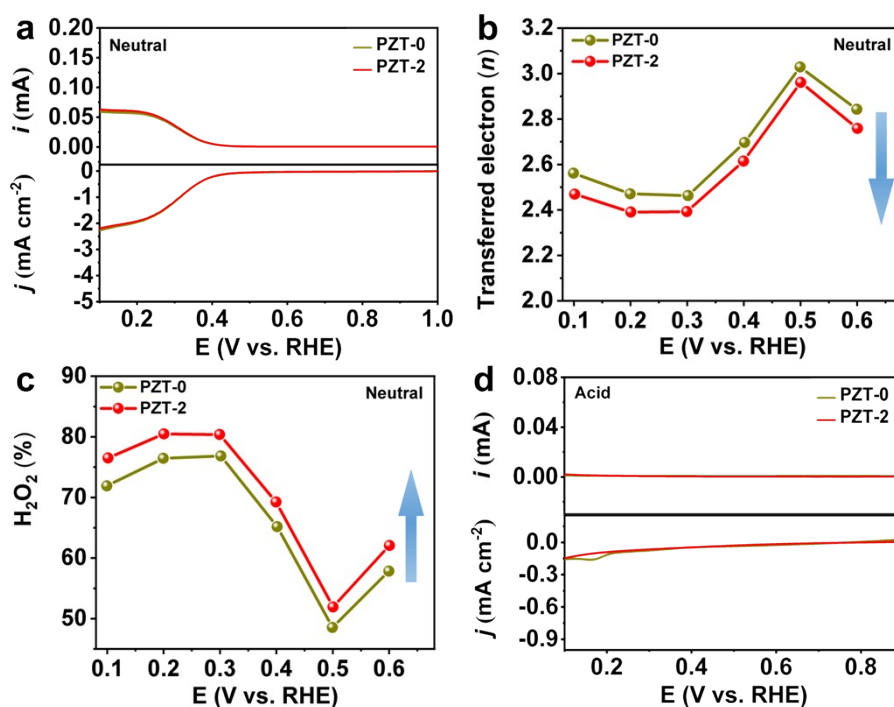
Fig. S17. In neutral media (0.1 M Na_2SO_4, pH ≈ 7), (a) LSV curves of PZT-0 and PZT-2 recorded at 1600 rpm with the scan rate of 10 mV s^{-1} (bottom part), accompanied by the associated H_2O_2 current on the ring electrode (upper part). (b) The calculated n, and (c) selectivity of H_2O_2 within the potential ranging from 0.6 to 0.1 V (*vs.* RHE). In acid media (0.05 M H_2SO_4, pH ≈ 1), (d) LSV curves of PZT-0 and PZT-2 recorded at 1600 rpm with the scan rate of 10 mV s^{-1} (bottom part), accompanied by the associated H_2O_2 current on the ring electrode (upper part).

Fig. S17a−c illustrates that under neutral conditions, both PZT catalysts presented inferior 2e$^-$ ORR performances to those in alkaline media (Fig. 2a−c of the main text), while polarized PZT-2 still performed better performance than that of unpolarized PZT-0, which could be due to the dynamic piezoelectric effect. However, in acid media, both of PZT-0 and PZT-2 showed almost no H_2O_2 currents on the ring electrode, possibly caused by the intrinsically inert 2e$^-$ ORR activity of PZT materials in acid environments (Fig. S17d).
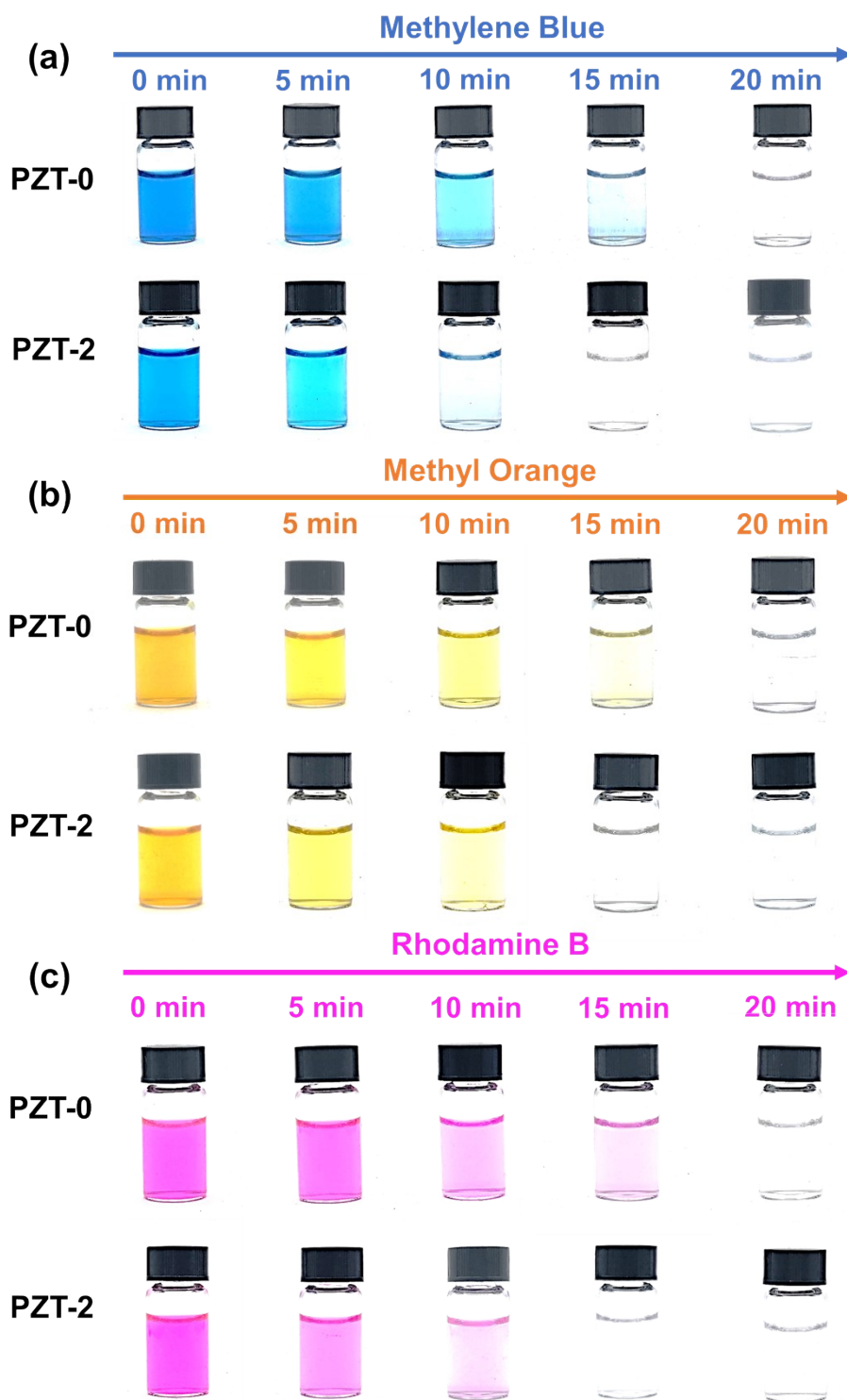
Fig. S18. Optical photos for the decolorization of (a) methylene blue, (b) methyl orange, and (c) rhodamine b with the increase of degradation time in the acidified catholytes of PZT-0 and PZT-2, which both on-site produced H_2O_2 through $2e^-$ ORR for 30 min.
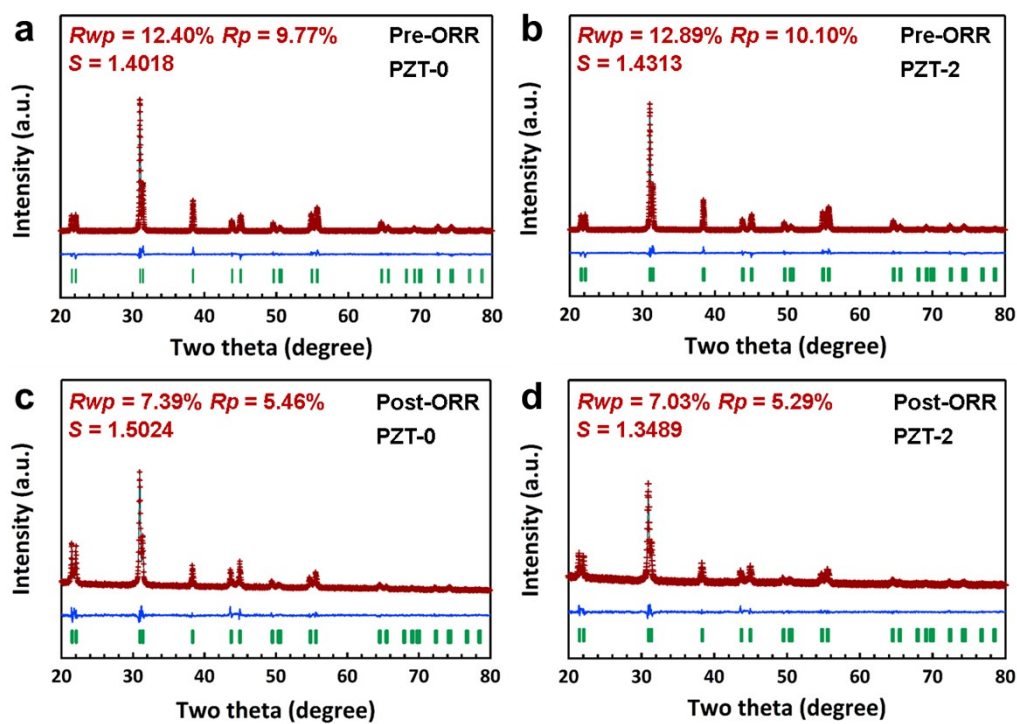
Fig. S19. Rietveld refinement for the XRD patterns of pre-ORR (a) PZT-0 and (b) PZT-2 powder catalysts, as well as post-ORR (c) PZT-0 and (d) PZT-2 ones.

As is shown in Fig. S19 and Table S7, the Rietveld refinement results unveil that both post-ORR PZT-0 and PZT-2 still well presented the PZT pure phase, and their structure parameters were almost the same, reflecting their high structural stability during ORR.

Table S7. Structural parameters and phase abundance for pre- and post-ORR PZT-0

Sample	Space group	Lattice parameters (Å)			Abundance (wt.%)
		a	*b*	*c*	
Pre-ORR PZT-0	*P*4mm	4.0342(5)	4.0342(5)	4.1386(8)	100
Pre-ORR PZT-2	*P*4mm	4.0339(5)	4.0339(5)	4.1395(4)	100
Post-ORR PZT-0	*P*4mm	4.0349(6)	4.0349(6)	4.1419(7)	100
Post-ORR PZT-2	*P*4mm	4.0348(4)	4.0348(4)	4.1423(5)	100

and PZT-2 powder catalysts refined from the experimental XRD profiles.
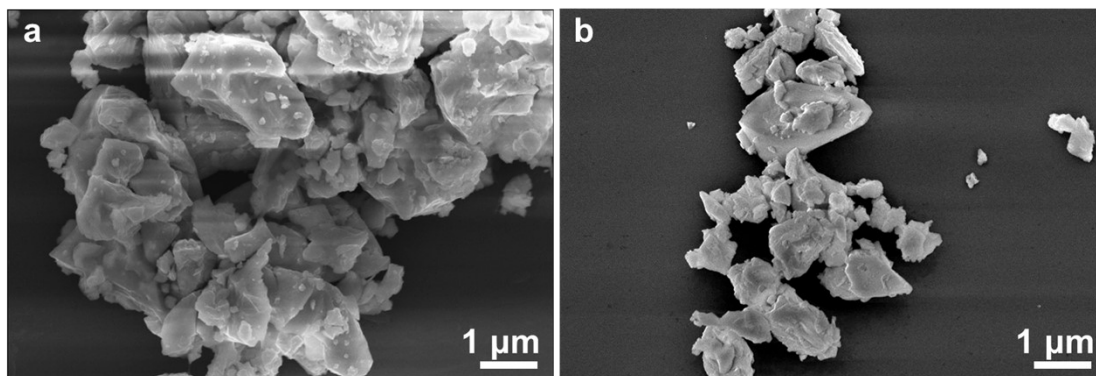
Fig. S20. FESEM images of post-ORR (a) non-piezoelectric PZT-0 and (b) piezoelectric PZT-2 powder catalysts.

Table S8. Elemental content of pre- and post-ORR non-piezoelectric PZT-0 and

Sample	Pb	Zr	Ti
PZT-0	1	0.49	0.49
PZT-2	1	0.48	0.47
Post-ORR PZT-0	1	0.45	0.49
Post-ORR PZT-2	1	0.46	0.49

piezoelectric PZT-2 powder catalysts determined by ICP-OES.
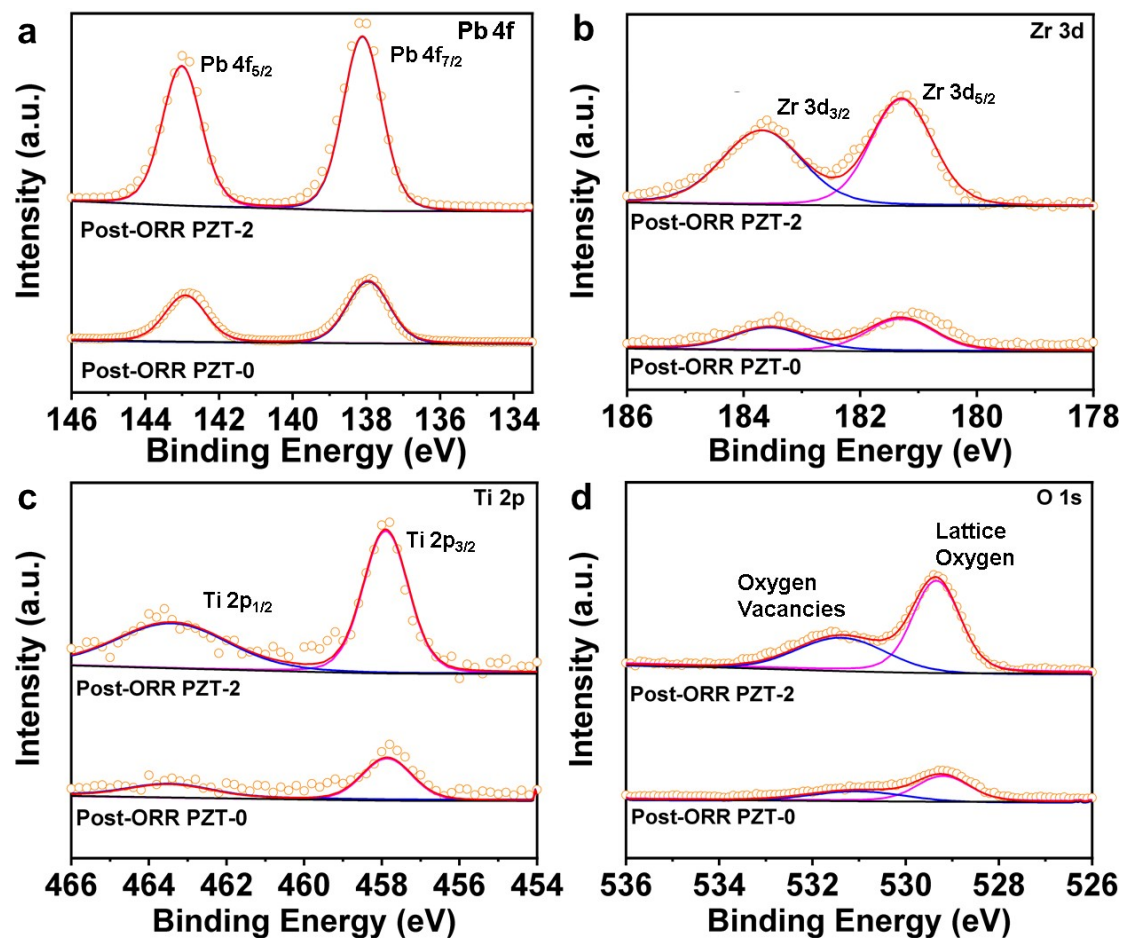
Fig. S21. High-resolution (a) Pb 4f, (b) Zr 3d, (c) Ti 2p, and (d) O 1s XPS spectra of post-ORR PZT-0 and post-ORR PZT-2 powder catalysts.

On one hand, both post-ORR PZT-0 and post-ORR PZT-2 catalysts still preserved their lead zirconate titanate phase without apparent change during the oxygen reduction process.[1] On the other hand, the fitted peaks of these two samples at the same position of binding energy suggested that they presented the same chemical environment after ORR.
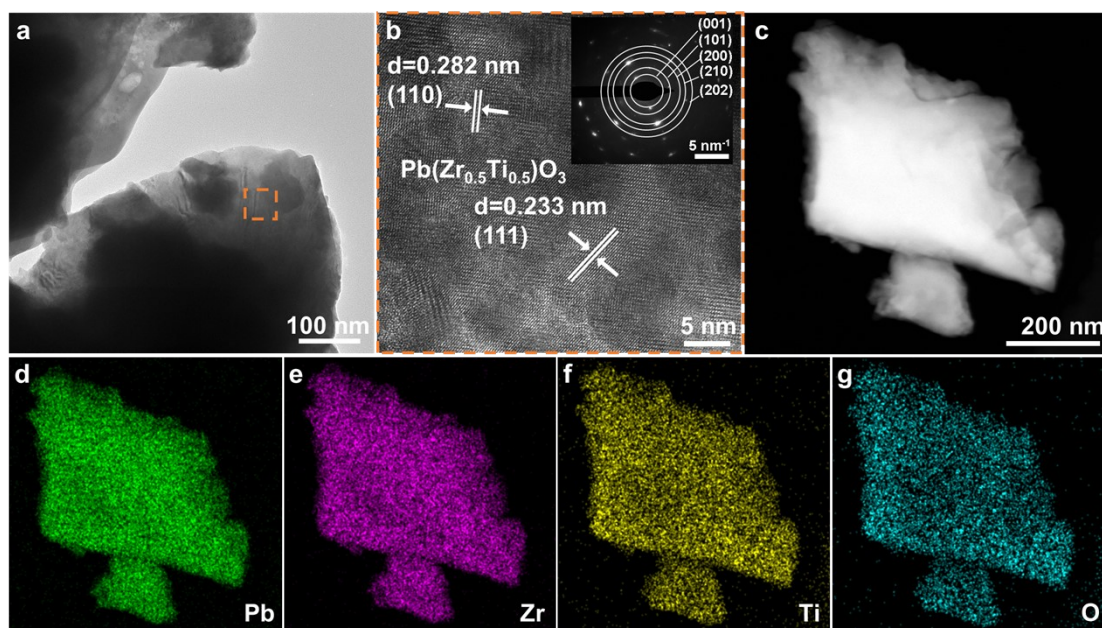
Fig. S22. (a) TEM image, and (b) HRTEM image with the inset of the SAED for post-ORR PZT-0 powder catalyst. (c) The HAADF-STEM pattern of representative PZT-0 particle together with the corresponding elemental mapping images of (d) Pb, (e) Zr, (f) Ti, and (g) O.

The identification of the lattice distances and the assignment of the crystalline facets reflected by the above HRTEM and SAED data confirmed the well-preserved lead zirconate titanate phase during the ORR process. Meanwhile, the HAADF-STEM pattern and the associated elemental mapping images illustrated that the distribution of all the elements for PZT-0 was still homogenously retained.
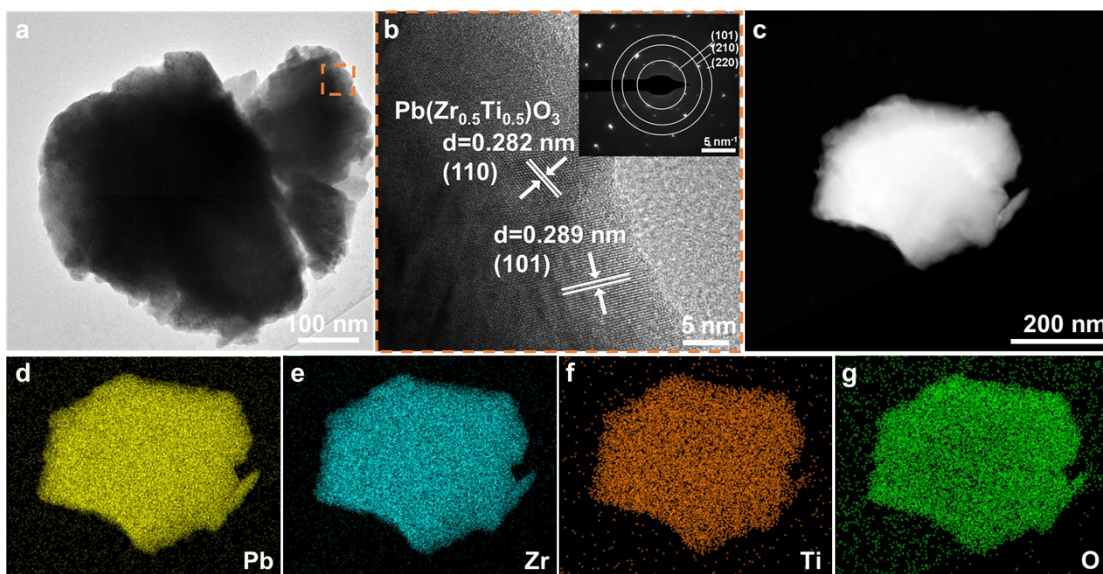
Fig. S23. (a) TEM image, and (b) HRTEM image with the inset of the SAED for post-ORR PZT-2 powder catalyst. (c) The HAADF-STEM pattern of representative PZT-0 particle together with the corresponding elemental mapping images of (d) Pb, (e) Zr, (f) Ti, and (g) O.

On one hand, the identification of the lattice distances and the assignment of the crystalline facets reflected by the above HRTEM and SAED data confirmed the well-preserved lead zirconate titanate phase during the ORR process. Meanwhile, the HAADF-STEM pattern and the associated elemental mapping images illustrated that the distribution of all the elements for PZT-2 was still homogenously retained. Therefore, it can be concluded that post-ORR PZT-0 and PZT-2 exhibited the same crystalline features and presence of elements.
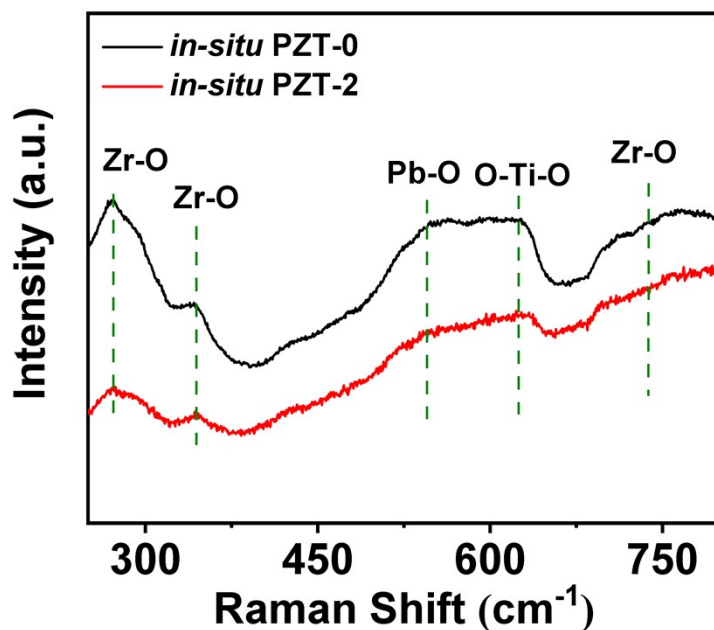
Fig. S24. Quasi *in-situ* Raman spectra of PZT-0 and PZT-2 freeze quenched at 0.4 V

vs. RHE after 12h ORR CA.

Both quasi *in-situ* PZT-0 and PZT-2 exhibited the same bands as those of *in-situ* Raman

results identified in a previous work on PZT catalyst for ORR.[1] This demonstrates that

PZT-0 and PZT-2 retained their original lead zirconate titanate phase during the ORR

process.

Table S9. d_{33} of PZT-2 ceramic tablet before and after 12 h ORR CA at 0.4 V *vs.* RHE

Sample	d_{33} (pC N^{-1})
Before ORR	-50
After ORR	-50

in the O$_2$-saturated 0.1 M KOH.

To probe the stability of piezoelectric behavior for the PZT catalyst during the ORR process, we directly ran a 12 h CA test for the starting ceramic tablet of polarized PZT-2 at a constant potential of 0.4 V (*vs.* RHE) in the O$_2$-saturated 0.1 M KOH electrolyte which was stirred at the rate of 1600 rpm (simulating the dynamic situations measured by RRDE). The post-ORR PZT-2 ceramic tablet exhibited the same d_{33} as that before electrochemistry treatment, signifying its excellent piezoelectric stability during electroreduction of O$_2$.
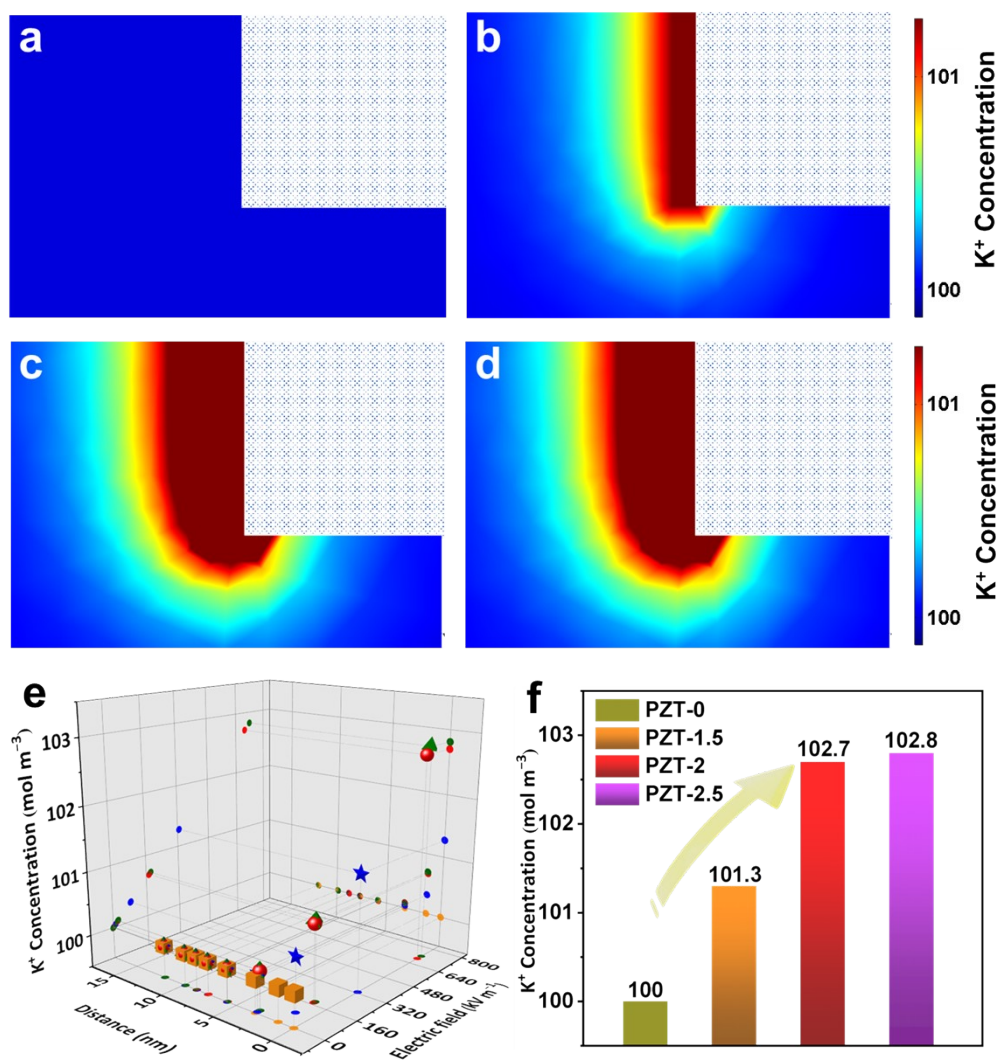
Fig. S25. The FEA simulation of K^+ density (unit: mol m^{-3}) mapping images at the immediate vicinity of (a) PZT-0, (b) PZT-1.5, (c) PZT-2, and (d) PZT-2.5, where the rectangles in the upper right corner of mapping images represent the associated ceramic catalysts. (e) The derived OH$^-$ concentration distribution as a function of the piezoelectricity-induced electric field intensity and the distance from the surface of PZT-0 (cube), PZT-1.5 (star), PZT-2 (sphere), and PZT-2.5 (tetrahedron) models. (f) The corresponding specific K^+ concentration values in the Helmholtz layer of the electric double layers (EDLs) directly adjacent to the surface of these four PZT models.
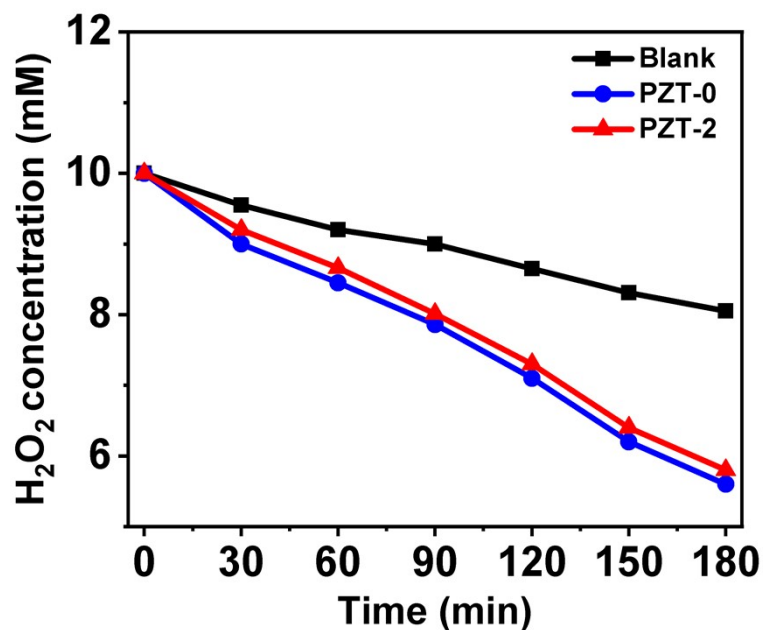
Fig. S26. Dynamic PDR measurements of non-piezoelectric PZT-0 and piezoelectric PZT-2, which were operated in the same reaction solution as the one utilized in the steady-state test (Fig. S13), while the solution herein was continuously stirred at a speed of 1600 rpm.

The PZT-2 catalyst always kept a higher H_2O_2 concentration in the reaction solution than that of PZT-0, proving the dynamic piezoelectric effect on maintaining the formed products from $2e^-$ ORR.
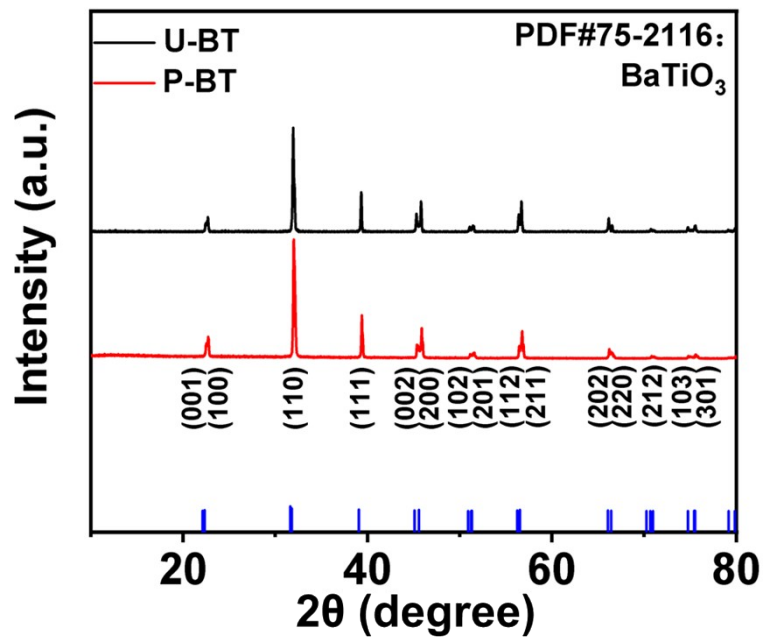
Fig. S27. XRD profiles of non-piezoelectric U-BT and piezoelectric P-BT powder catalysts. Both of them can be well-indexed to the BaTiO$_3$ (BT) phase.
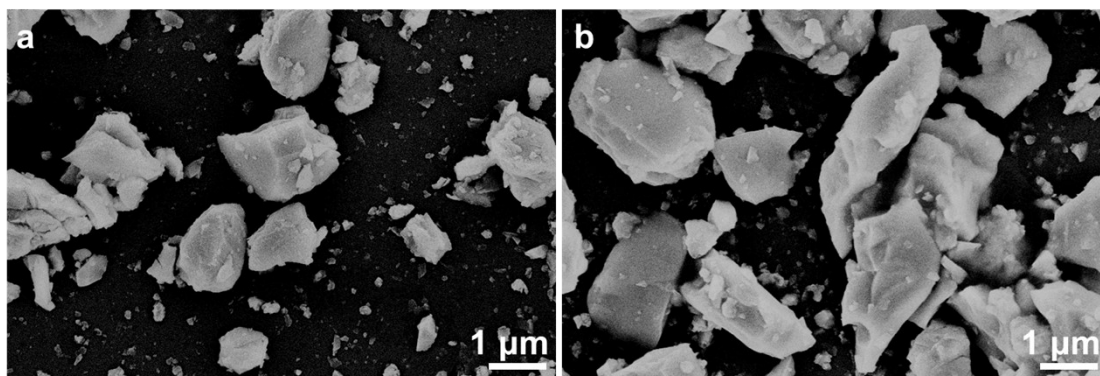
Fig. S28. FESEM images of (a) non-piezoelectric U-BT and (b) piezoelectric P-BT powder catalysts.

Table S10. Elemental content of non-piezoelectric U-BT and piezoelectric P-BT

Sample	Ba	Ti
U-BT	0.95	1
P-BT	1	1

powder catalysts determined by ICP-OES.

The ICP-OES results presented herein prove that before and after polarizing treatment,

BT ($BaTiO_3$) samples still preserved their well-defined composition.

Table S11. d_{33} of U-BT and P-BT in the form of starting ceramic tablets and ground powders (deposited on insulating side of FTO slide), respectively, treated under

Sample	Polarization electric field (kV mm^{-1})	d_{33} (pC N^{-1}) Tablet	d_{33} (pC N^{-1}) Powder
U-BT	0	0	0
P-BT	1.5	-25	-0.9

different polarization electric fields.
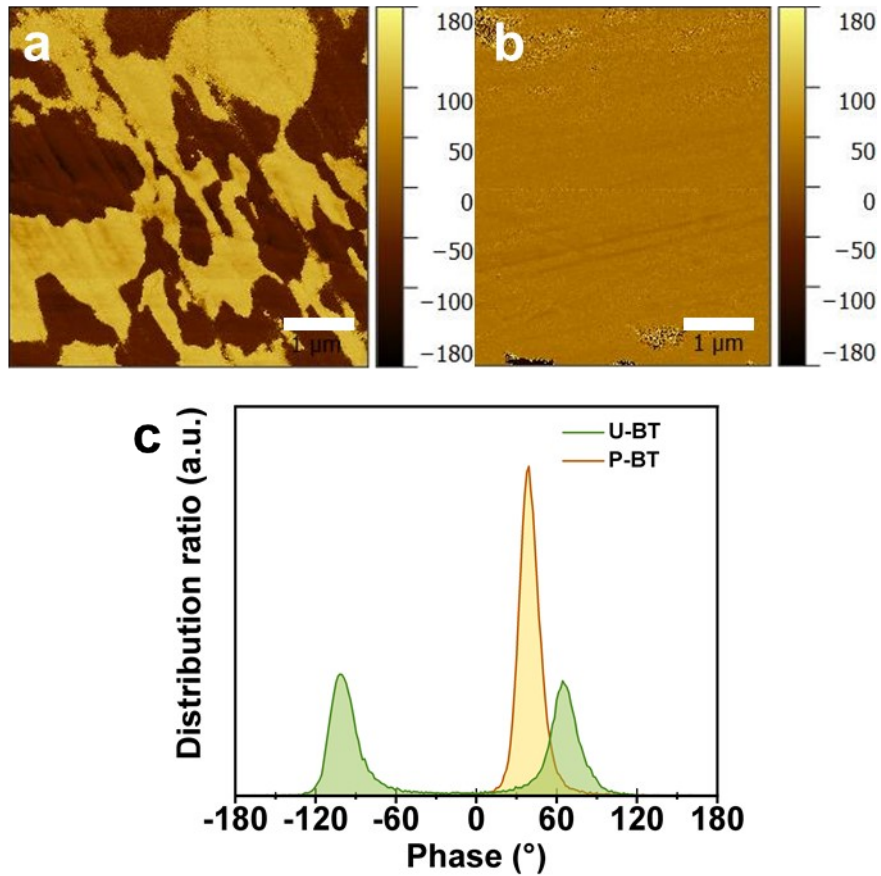
Fig. S29. PFM images of (a) the unpolarized U-BT ceramic tablet and (b) polarized P-BT tablet, as well as (c) their corresponding phase distribution diagram. Scale bar: 1 μm.

Apparently, after the polarizing treatment, distinctly more concentrated and ordered the electric domain distribution can be found in the P-BT ceramic tablet, demonstrating its piezoelectric performance was accordingly enhanced.
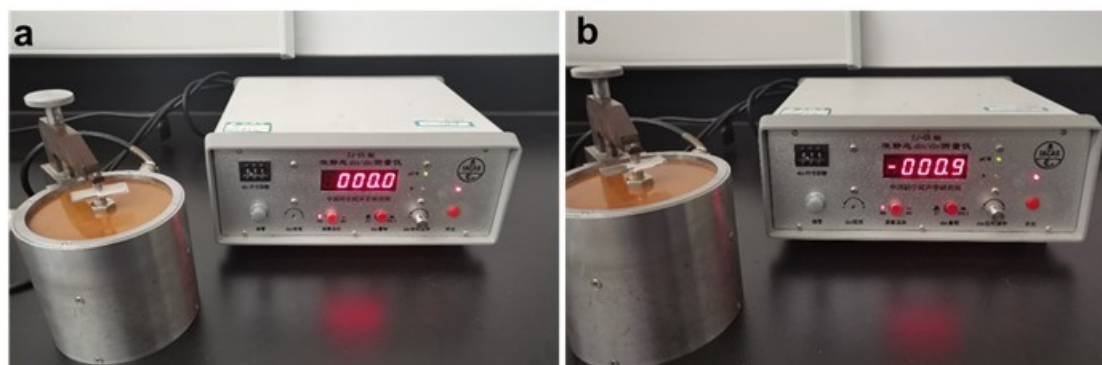
Fig. S30. d_{33} tests of the ground (a) U-BT and (b) P-BT powder samples.

Note the starting BT tablets were ground into powders as the ORR catalysts, which were deposited on FTO substrates to measure their d_{33} behaviors in the form of powders (details in **Supplementary experimental details**). The results presented in this figure confirm that the powder P-BT can still show the piezoelectric activity, while no piezoelectricity can be found in U-BT powder catalysts.
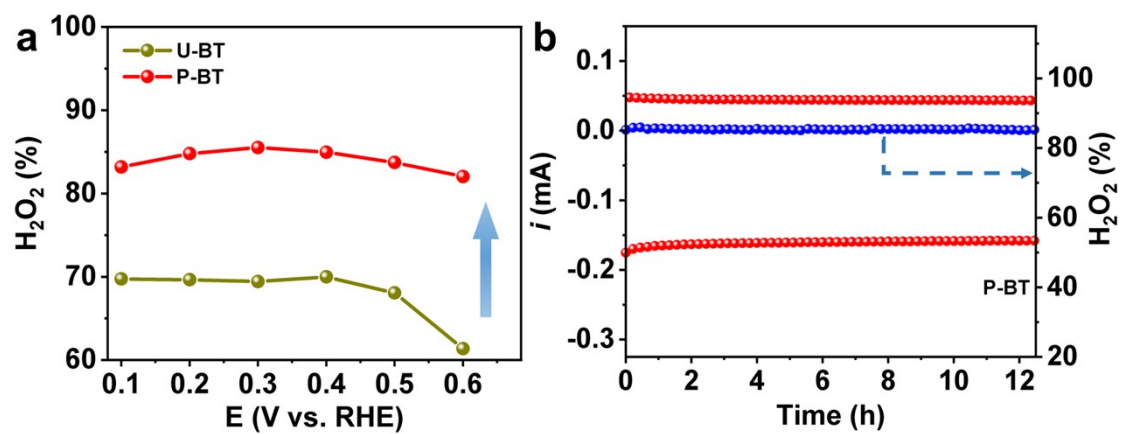
Fig. S31. (a) The calculated selectivity of H_2O_2 for U-BT and P-BT within the potential ranging from 0.6 to 0.1 V (*vs.* RHE). (a) CA stability tests of P-BT at a fixed disk potential of 0.4 V *vs*. RHE.
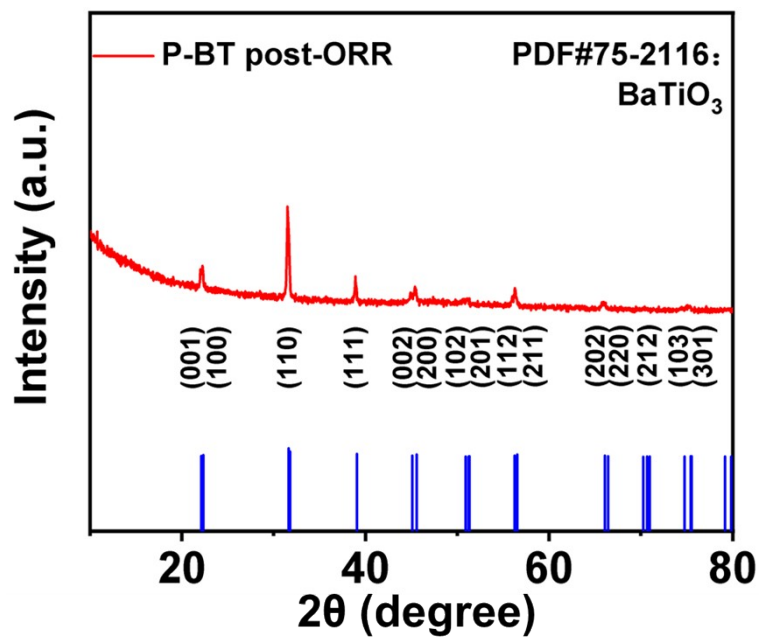
Fig. S32. XRD profile of post-ORR piezoelectric P-BT powder catalyst. All the diffraction peaks can still be well-indexed to the BaTiO$_3$ phase (PDF #75-2116), which is identical to those of the same sample before the electrochemistry, indicating that the crystalline structure was maintained well for P-BT during the ORR process.

Table S12. Elemental content of pre- and post-ORR piezoelectric P-BT powder

Sample	Ba	Ti
P-BT	1	1
Post-ORR P-BT	0.99	1

catalysts determined by ICP-OES..

The ICP-OES results presented here prove that the content of P-BT maintained well after the ORR stability test.

Table S13. Simulated surface potentials of the non-piezoelectric U-BT and piezoelectric P-BT models under the stresses induced by fluid rotating (the same speed as the RRDE rotating value for ORR measurement).

Sample	Surface potential (V)
U-BT	0
P-BT	-4.48 x 10^{-4}
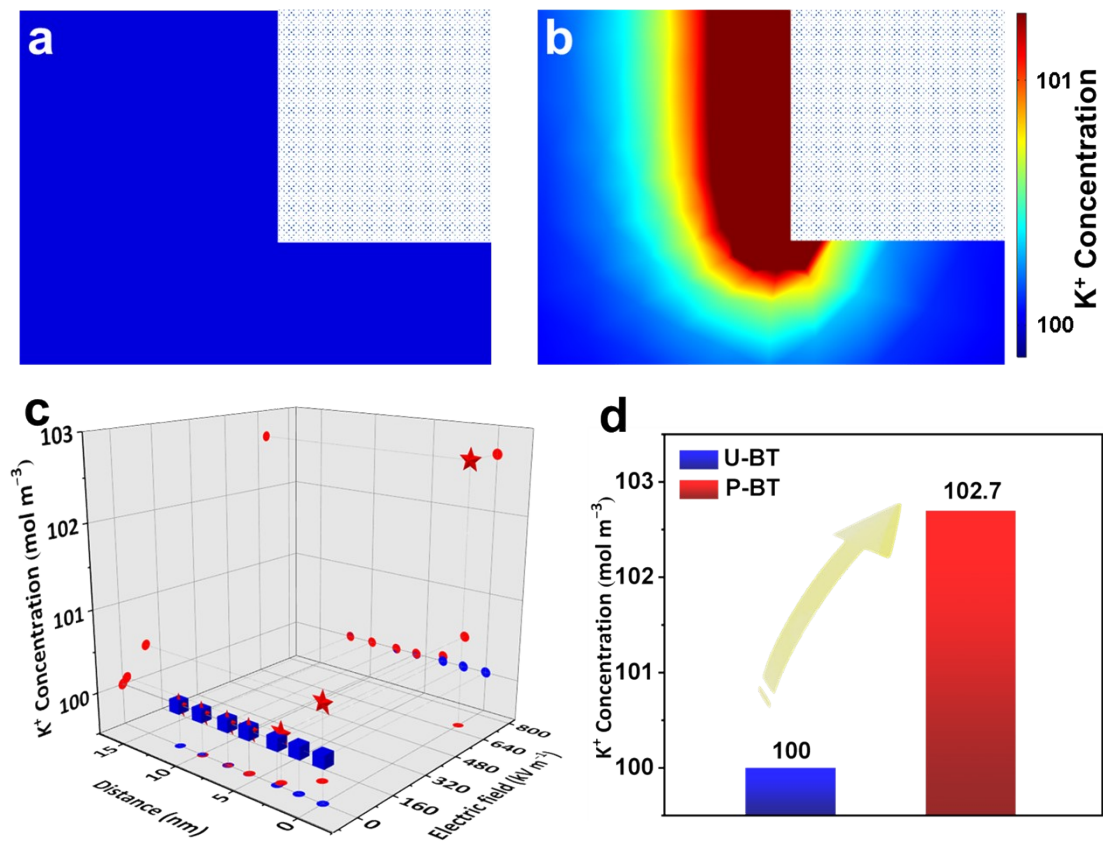
Fig. S33. The FEA simulation of K^+ density (unit: mol m^{-3}) mapping images at the immediate vicinity of (a) U-BT and (b) P-BT, where the rectangles in the upper right corner of mapping images represent the associated ceramic catalysts. (c) The derived K^+ concentration distribution as a function of the piezoelectricity-induced electric field intensity and the distance from the surface of U-BT (cube) and P-BT (star), as well as (d) the specific concentration values in the Helmholtz layer of the EDLs directly adjacent to the surface of U-BT and P-BT.
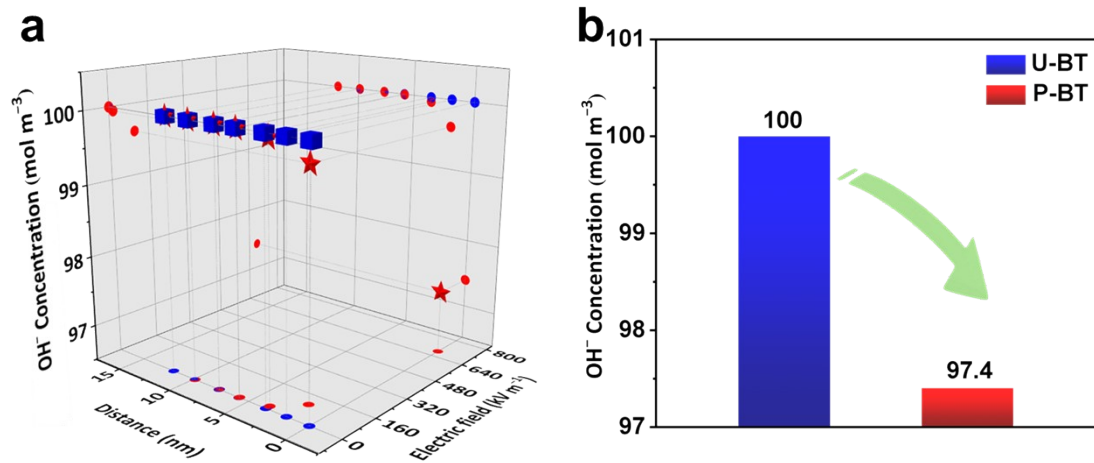
Fig. S34. (a) The FEA-simulated OH$^-$ concentration distribution as a function of the piezoelectricity-induced electric field intensity and the distance from the surface of U-BT (cube) and P-BT (star), as well as (b) the specific concentration values in the Helmholtz layer of the EDLs directly adjacent to the surface of U-BT and P-BT.
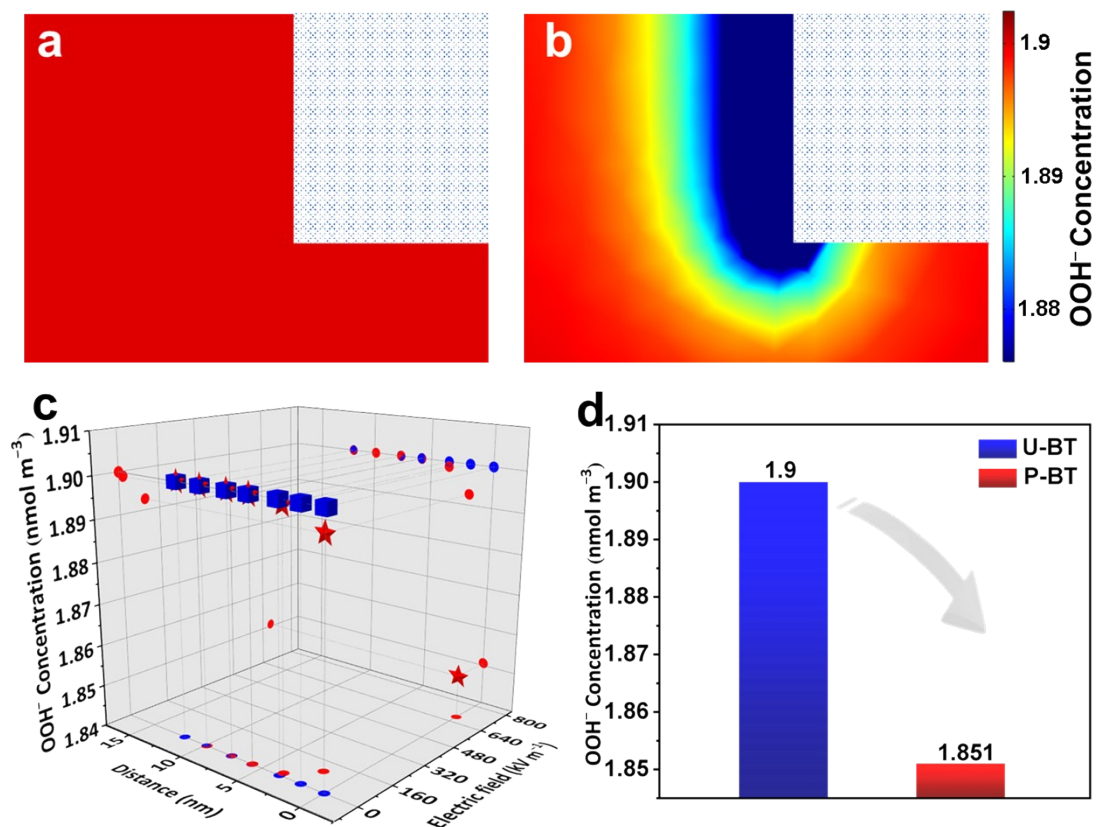
Fig. S35. The FEA simulation of OOH⁻ density (unit: nmol m⁻³) mapping images at the immediate vicinity of (a) U-BT and (b) P-BT, where the rectangles in the upper right corner of mapping images represent the associated ceramic catalysts. (c) The derived OOH⁻ concentration distribution as a function of the piezoelectricity-induced electric field intensity and the distance from the surface of U-BT (cube) and P-BT (star), as well as (d) the specific concentration values in the Helmholtz layer of the EDLs directly adjacent to the surface of U-BT and P-BT.
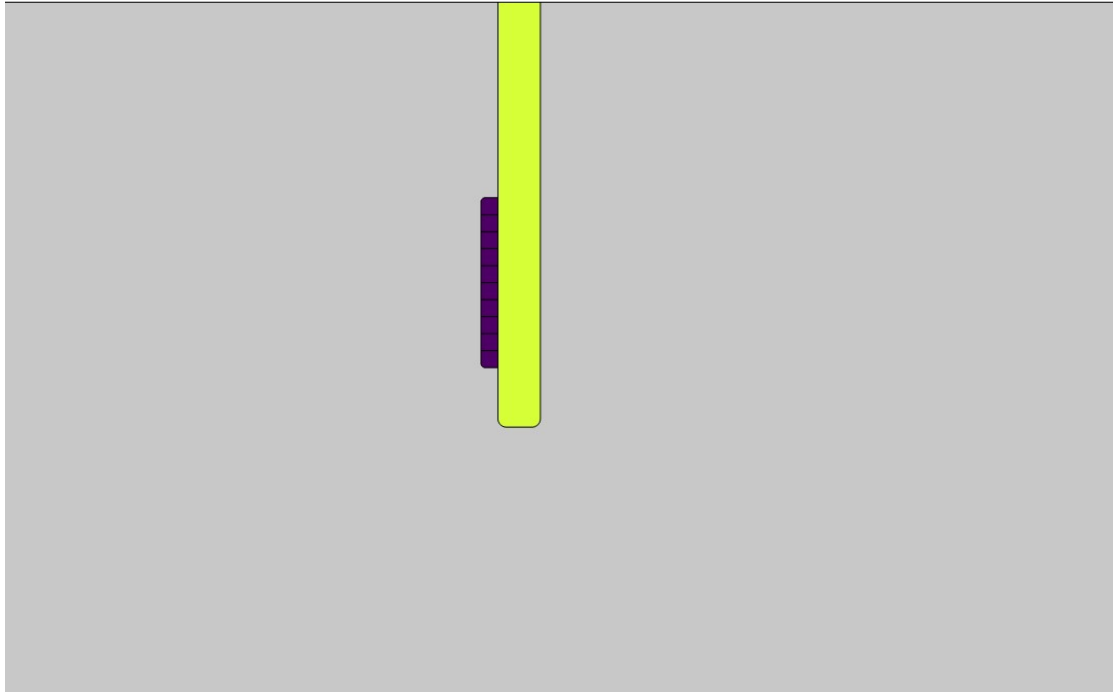
Fig. S36. Simplified two-dimensional particle sample model (dark purple area) supported onto electrode (yellow area) for piezoelectric behavior simulations.

Table S14. Specific parameter settings for piezoelectric behavior simulations.

Steady-state average velocity at inlet	8.38 m s^{-1}
Channel height	2 x 10^{-4} m
Channel width	3 x 10^{-4} m
Radius of rotation	0.05 m
Rotating speed	1600 rpm
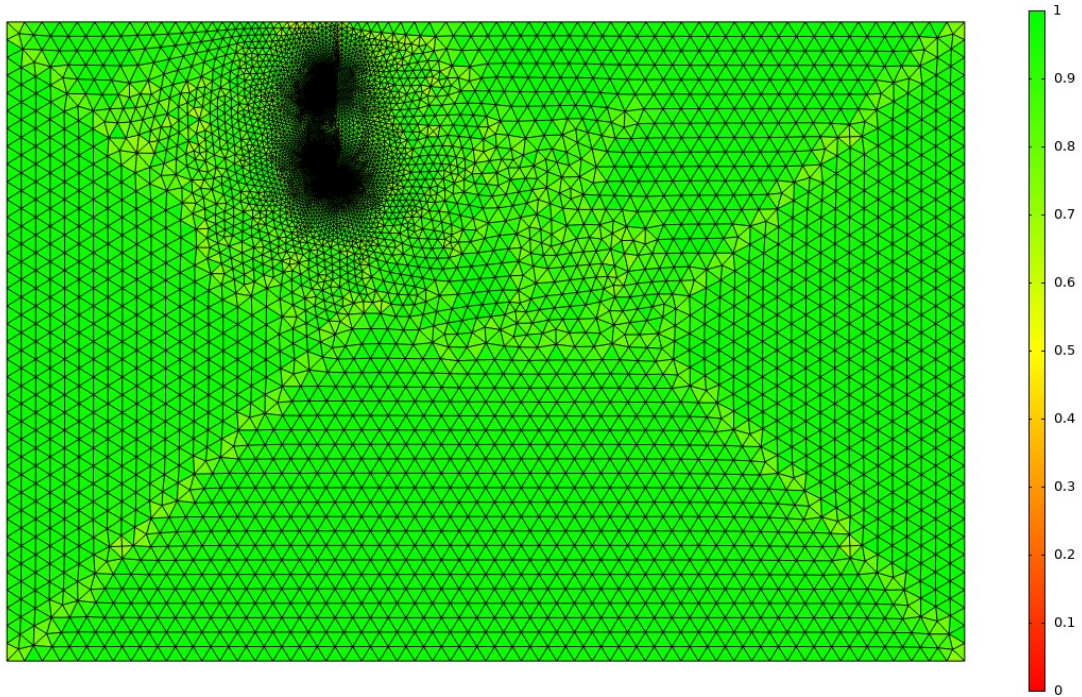
Fig. S37. Meshing results of piezoelectric behaviors by COMSOL Multiphysics® 5.5 software.
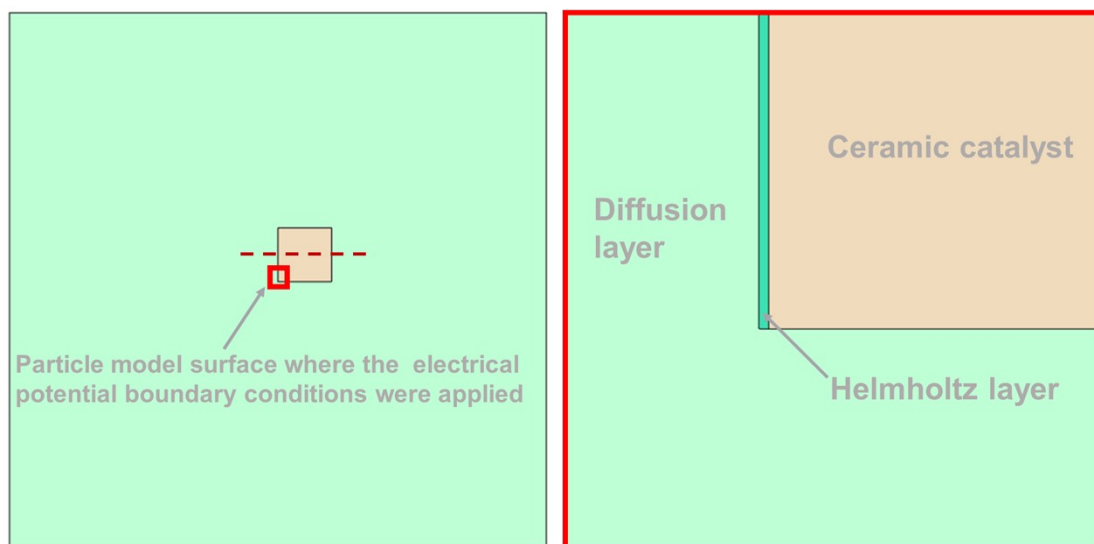
Fig. S38. The calculation model for simulations of ions concentration within the electric double layers region (dark green: Helmholtz layer, light green: diffusion layer) of a ceramic catalyst (PZT and BT) (light orange). Note that at the middle height (marked by a dark red dash line) of the PZT and BT models in the current simulation, the function of electric fields and K^+/OH^-/OOH^- concentration with the distance away from the PZT and BT surface was obtained, as depicted in Figs. 3−4 of the main text, as well as Figs. S25, S33−S35.

Table S15. Specific parameter settings for simulations of ion (K^+, OH^-, and OOH^-) concentration.

For PZT samples:

Electrostatics field	Surface potential of piezoceramics(V)			
	0 (PZT-0)	-6.98×10^{-4} (PZT-1.5)	-7.07×10^{-4} (PZT-2)	-7.34×10^{-4} (PZT-2.5)
Transport of diluted species field	Concentration(mol L^{-1})		Charge	
	0.1 (K)	0.1 (OH)	1.9×10^{-12} (OOH)	+1 (K)	-1 (OH)	-1 (OOH)

For BT samples:

Electrostatics field	Surface potential of piezoceramics(V)			
	0 (U-BT)	-4.48×10^{-4} (P-BT)		
Transport of diluted species field	Concentration(mol L^{-1})		Charge	
	0.1 (K)	0.1 (OH)	1.9×10^{-12} (OOH)	+1 (K)	-1 (OH)	-1 (OOH)

Herein we assume all Zr and Ti atoms of a PZT, as well as all Ti atoms of a BT are the sites where OOH^- ions can be possibly absorbed during $2e^-$ ORR. Moreover, the density of PZT and BT is 7.75 and 5.67 g cm^{-3}, respectively,[38,39] while a PZT (BT) model used in the current work holds a volume of around 8 μm^3. Also, the electrolyte volume employed in our experiments is 100 mL. Thus, the pristine concentration of OOH^- ions (1.9×10^{-12} mol L^{-1}) in our calculations was determined based on the possible maximum amounts of OOH^- adsorbed by a PZT (or a BT) unit in 100 mL electrolyte.
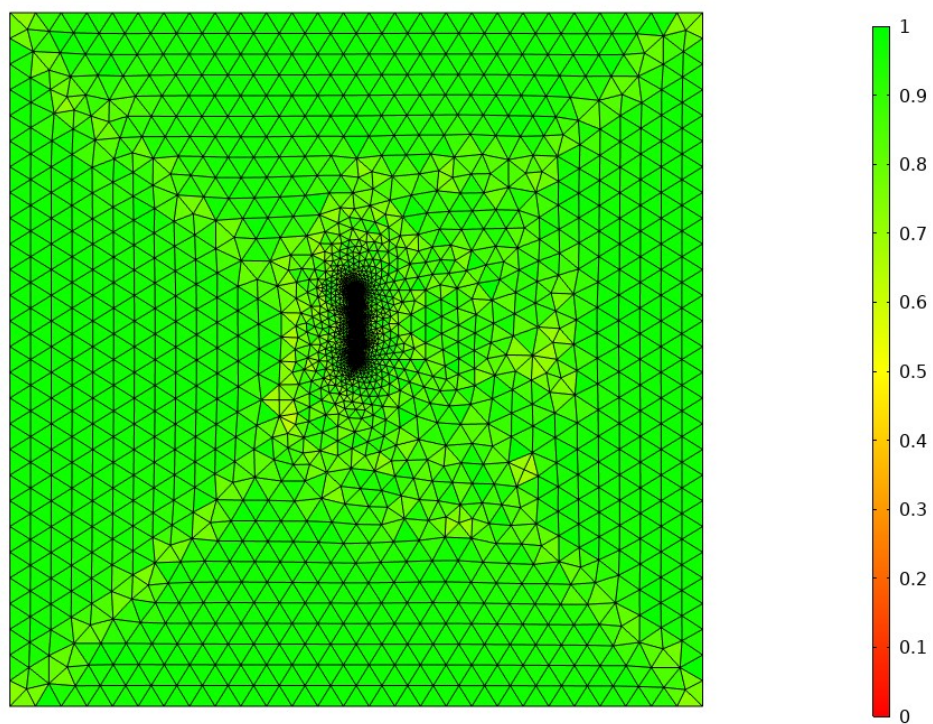
Fig. S39. Meshing results for simulations of ion concentration (K$^+$, OH$^-$, and OOH$^-$) by COMSOL Multiphysics® 5.5 software.

References

[1] Z. Chen, J. Wu, Z. Chen, H. Yang, K. Zou, X. Zhao, R. Liang, X. Dong, P. W. Menezes and Z. Kang, *Angew. Chem. Int. Ed.*, 2022, **61**, e202200086.

[2] A. E. Pasto and R. A. Condrate Sr., *J. Am. Ceram. Soc.*, 1973, **56**, 436–438.

[3] J. Rouquette, J. Haines, V. Bornand, M. Pintard, Ph. Papet, B. Bonnet and F. A. Gorelli, *Solid State Sci.*, 2003, **5**, 451–457.

[4] C. D. E. Lakeman, Z. Xu, and D. A. Payne, *J. Mater. Res.*, 1995, **10**, 2042–2051.

[5] M. Baibarac, M. Sima, E. Matei, I. Pasuk and L. Mihut, *Phys. Status Solidi A*, 2014, **211**, 200–205.

[6] K. K. Bajpai, K. Sreenivas, A. K. Gupta and A. K. Shukla, *Ceram. Int.*, 2019, **45**, 14111–14120.

[7] M. Nishide, H. Takeuchi, T. Tai, T. Katoda, S. Yokoyama, S. Yasui, H. Funakubo, K. Nishida and T. Yamamoto. *Integr. Ferroelectr.*, 2009, **112**, 33–41.

[8] W. P. Barros, Q. Wei, G. Zhang, S. Sun, M. R. V. Lanza and A. C. Tavares, *Electrochim. Acta*, 2015, **162**, 263–270.

[9] Z. Xu, J. Liang, Y. Wang, K. Dong, X. Shi, Q. Liu, Y. Luo, T. Li, Y. Jia, A. M. Asiri, Z. Feng, Y. Wang, D. Ma and X. Sun, *ACS Appl. Mater. Interfaces*, 2021, **13**, 33182–33187.

[10] S. Thundiyil, S. Kurungot and R. N. Devi, *ACS Appl. Mater. Interfaces*, 2021, **13**, 382–390.

[11] J. F. Carneiro, M. J. Paulo, M. Siaj, A. C. Tavares and M. R. V. Lanza, *J. Catal.*, 2015, **332**, 51–61.

[12] J. F. Carneiro, M. J. Paulo, M. Siaj, A. C. Tavares and M. R. V. Lanza, *ChemElectroChem*, 2017, **4**, 508–513.

[13] R. R. Mahalik and P. Parhi, *Mater. Today: Proc.*, 2021, **43**, 3261–3267.

[14] H. Xiao, B. Li, M. Zhao, Y. Li, T. Hu, J. Jia and H. Wu, *Chem. Commun.*, 2021, **57**, 4118–4121.

[15] M. H. M. T. Assumpção, A. Moraes, R. F. B. De Souza, M. L. Calegaro, M. R. V. Lanza, E. R. Leite, M. A. L. Cordeiro, P. Hammerd and M. C. Santos, *Electrochim. Acta*, 2013, **111**, 339–343.

[16] M. Wang, N. Zhang, Y. Feng, Z. Hu, Q. Shao and X. Huang, *Angew. Chem., Int. Ed.*, 2020, **59**, 14373–14377.

[17] J. Huang, J. Chen, C. Fu, P. Cai, Y. Li, L. Cao, W. Liu, P. Yu, S. Wei, Z. Wen and J. Li, *ChemSusChem*, 2020, **13**, 1496–1503.

[18] S. V. Venkatesan, A. H. B. Mostaghimi, V. Thangadurai and S. Siahrostami, *Electrochem. Sci. Adv.*, 2022, e2100140.

[19] J. F. Carneiro, R. S. Rocha, P. Hammer, R. Bertazzoli and M. R. V. Lanza, *Appl. Catal. A*, 2016, **517**, 161–167.

[20] F. Xia, B. Li, Y. Liu, Y. Liu, S. Gao, K. Lu, J. Kaelin, R. Wang, T. J. Marks and Y. Cheng, *Adv. Funct. Mater.*, 2021, **31**, 2104716.

[21] X. Long, Y. Ling, C. Chang, F. Luo and Z. Yang, *Chem. Commun.*, 2022, **58**, 9782–9785.

[22] C. Da, R, Li, H. Guo, S. Liang, H. Shen, T. Thomas and M. Yang, *Dalton Trans.*, 2021, **50**, 5416–5419.

[23] X. Xu, X. Yin, J. Fu and D. Ke, *Chem. Eur. J.*, 2021, **27**, 14451–14460.

[24] C. Zhang, R. Lu, C. Liu, J. Lu, Y. Zou, L. Yuan, J. Wang, G. Wang, Y. Zhao and C. Yu, *Adv. Sci.*, 2022, **9**, 2104768.

[25] Q. Yuan, J. Zhao, D. H. Mok, Z. Zheng, Y. Ye, C. Liang, L. Zhou, S. Back and K. Jiang, *Nano Lett.*, 2022, **22**, 1257–1264.

[26] Y. Ji, Y. Liu, B. Zhang, Z. Xu, X. Qi, X. Xu, L. Ren, Y. Du, J. Zhong and S. X. Dou, *J. Mater. Chem. A*, 2021, **9**, 21340–21346.

[27] R. D. Ross, H. Sheng, A. Parihar, J. Huang and S. Jin, *ACS Catal.*, 2021, **11**, 12643–12650.

[28] H. Sheng, E. D. Hermes, X. Yang, D. Ying, A. N. Janes, W. Li, J. R. Schmidt and S. Jin, *ACS Catal.*, 2019, **9**, 8433–8442.

[29] H. Sheng, A. N. Janes, R. D. Ross, D. Kaiman, J. Huang, B. Song, J. R. Schmidt and S. Jin, *Energy Environ. Sci.*, 2020, **13**, 4189–4203.

[30] Z. Lu, G. Chen, S. Siahrostami, Z. Chen, K. Liu, J. Xie, L. Liao, T. Wu, D. Lin, Y. Liu, T. F. Jaramillo, J. K. Nørskov and Y. Cui, *Nat. Catal.*, 2018, **1**, 156–162.

[31] Z. Zheng, Y. H. Ng, D. Wang and R. Amal, *Adv. Mater.*, 2016, **28**, 9949–9955.

[32] K. Jiang, S. Back, A. J. Akey, C. Xia, Y. Hu, W. Liang, D. Schaak, E. Stavitski, J. K. Nørskov, S. Siahrostami and H. Wang, *Nat. Commun.*, 2019, **10**, 3997.

[33] Y. Sun, L. Silvioli, N. R. Sahraie, W. Ju, J. Li, A. Zitolo, S. Li, A. Bagger, L. Arnarson, X. Wang, T. Moeller, D. Bernsmeier, J. Rossmeisl, F. Jaouen and P. Strasser, *J. Am. Chem. Soc.*, 2019, **141**, 12372–12381.

[34] Y. Zheng, X. Xu, J. Chen and Q. Wang, *Appl. Catal. B*, 2021, **285**, 119788.

[35] Y. Wang, R. Shi, L. Shang, G. I. N. Waterhouse, J. Zhao, Q. Zhang, L. Gu, T. Zhang, *Angew. Chem. Int. Ed.*, 2020, **59**, 13057–13062.

[36] J. Frantti, J. Lappalainen, S. Eriksson, V. Lantto, S. Nishio, M. Kakihana, S. Ivanov and H. Rundlöf, *Jpn. J. Appl. Phys.*, 2000, **39**, 5697–5703.

[37] Y. Xu, Y. Wang, A. Liu, W. Shi, G. Hu, S. Li, H. Deng and N. Dai, *Chinese Phys. Lett.*, 2020, **37**, 026801.

[38] A. C. Dent, L. J. Nelson, C. R. Bowen, R. Stevens, M. Cain and M. Stewart, *J. Eur. Ceram. Soc.*, 2005, **25**, 2387–2391.

[39] T. Karaki, K. Yan, T. Miyamoto and M. Adachi, *Jpn. J. Appl. Phys.*, 2007, **46**, L97.